Influences of Recent Particle Formation on Southern Ocean Aerosol Variability and Low Cloud Properties

Isabel L. McCoy[1], Christopher S. Bretherton[1,1], Robert Wood[1,1], Cynthia H. Twohy[2,2], Andrew Gettelman[3,3], Charles Bardeen[3,3], Darin W. Toohey[4,4], and Isabel L. McCoy[1]

[1]University of Washington
[2]Northwest Research Associates
[3]National Center for Atmospheric Research (UCAR)
[4]University of Colorado Boulder

July 7, 2023

Abstract

Controls on pristine aerosol over the Southern Ocean (SO) are critical for constraining the strength of global aerosol indirect forcing. Observations of summertime SO clouds and aerosols in synoptically varied conditions during the 2018 SOCRATES aircraft campaign reveal novel mechanisms influencing pristine aerosol-cloud interactions. The SO free troposphere (3-6 km) is characterized by widespread, frequent new particle formation events contributing to much larger concentrations ([?] 1000 mg-1) of condensation nuclei (diameters > 0.01 μm) than in typical sub-tropical regions. Synoptic-scale uplift in warm conveyor belts and sub-polar vortices lifts marine biogenic sulfur-containing gases to free-tropospheric environments favorable for generating Aitken-mode aerosol particles (0.01-0.1 μm). Free-tropospheric Aitken particles subside into the boundary layer, where they grow in size to dominate the sulfur-based cloud condensation nuclei (CCN) driving SO cloud droplet number concentrations (Nd ˜ 60-100 cm-3). Evidence is presented for a hypothesized Aitken-buffering mechanism which maintains persistently high summertime SO Nd against precipitation removal through CCN replenishment from activation and growth of boundary layer Aitken particles. Nudged hindcasts from the Community Atmosphere Model (CAM6) are found to underpredict Aitken and accumulation mode aerosols and Nd, impacting summertime cloud brightness and aerosol-cloud interactions and indicating incomplete representations of aerosol mechanisms associated with ocean biology.

Influences of Recent Particle Formation on Southern Ocean Aerosol Variability and Low Cloud Properties

Isabel L. McCoy[1], Christopher S. Bretherton[1], Robert Wood[1], Cynthia H. Twohy[2], Andrew Gettelman[3], Charles G. Bardeen[3], and Darin W. Toohey[4]

[1] Atmospheric Sciences, University of Washington, Seattle, WA, USA, [2] Northwest Research Associates, Redmond, WA, USA, [3] National Center for Atmospheric Research, Boulder, CO, USA, [4]Atmospheric and Oceanic Sciences, University of Colorado, Boulder, CO, USA.

Corresponding author: Isabel L. McCoy (imccoy@ucar.edu)

Key Points:

- Summertime Southern Ocean free tropospheric aerosol number is dominated by Aitken particles recently generated through synoptic uplift.
- Entrained Aitken aerosols buffer Southern Ocean boundary layer cloud condensation nuclei and cloud droplets against precipitation removal.
- Southern Ocean cloud droplet number is too low in the CAM6 climate model due to inadequate free tropospheric production of Aitken aerosols.

Abstract

Controls on pristine aerosol over the Southern Ocean (SO) are critical for constraining the strength of global aerosol indirect forcing. Observations of summertime SO clouds and aerosols in synoptically varied conditions during the 2018 SOCRATES aircraft campaign reveal novel mechanisms influencing pristine aerosol-cloud interactions. The SO free troposphere (3-6 km) is characterized by widespread, frequent new particle formation events contributing to much larger concentrations ($\geq$ 1000 mg^{-1}) of condensation nuclei (diameters > 0.01 μm) than in typical sub-tropical regions. Synoptic-scale uplift in warm conveyor belts and sub-polar vortices lifts marine biogenic sulfur-containing gases to free-tropospheric environments favorable for generating Aitken-mode aerosol particles (0.01-0.1 μm). Free-tropospheric Aitken particles subside into the boundary layer, where they grow in size to dominate the sulfur-based cloud condensation nuclei (CCN) driving SO cloud droplet number concentrations (N_d ~ 60-100 cm^{-3}). Evidence is presented for a hypothesized Aitken-buffering mechanism which maintains persistently high summertime SO N_d against precipitation removal through CCN replenishment from activation and growth of boundary layer Aitken particles. Nudged hindcasts from the Community Atmosphere Model (CAM6) are found to underpredict Aitken and accumulation mode aerosols and N_d, impacting summertime cloud brightness and aerosol-cloud interactions and indicating incomplete representations of aerosol mechanisms associated with ocean biology.

Plain Language Summary

The remote Southern Ocean (SO) is a unique analogue to pre-industrial environments due to limited continental and anthropogenic influences. Understanding how aerosols are produced in this region and their influence on cloud droplet concentrations is vital for understanding how much sunlight these clouds reflect to space, which affects ocean temperatures and global climate. This is a key uncertainty in modeling past and future climate change due to anthropogenic emissions of carbon dioxide and other pollutants. To understand this pristine environment, we analyze novel observations of SO clouds and aerosols from a summertime aircraft campaign. We present evidence for an aerosol production mechanism driven by synoptic storms and sourced from emissions of ocean biology. This mechanism produces a reservoir of small aerosols above cloud that subside into the marine boundary layer, where they grow into cloud-affecting sizes and control cloud droplet number. In addition to acting as a source of boundary layer aerosol, these small particles help SO clouds to resist precipitation depletion of cloud-affecting aerosol, maintaining surprisingly high cloud droplet number concentrations that help to keep present-day SO clouds persistently bright. This mechanism has important implications for understanding pre-industrial and other pristine environments and their response to anthropogenic aerosol.

1 Introduction

The Southern Ocean (SO) is our closest present-day (PD) analog to the pre-industrial (PI) state due to its pristine aerosol (Hamilton et al., 2014). It is also frequently cloudy, providing ample opportunity for aerosol-cloud interactions (ACI) to take place. Understanding the climate response to changes in anthropogenic aerosol (i.e. PI to PD states) will help to reduce the uncertainty in global climate model (GCM) climate sensitivity and improve climate predictions (Andreae et al., 2005; Forster, 2016). Aerosol-cloud interactions are the main contributor to uncertainty in total radiative forcing (Bellouin et al., 2020). Poor understanding of PI aerosol

state is a leading driver of this uncertainty (Carslaw et al., 2013), making observations in pristine locations that give us insight into PI aerosol and ACI doubly important. This was a central focus of the 2018 Southern Ocean Clouds Radiation and Aerosol Transport Experimental Study (SOCRATES) aircraft campaign that took place in the austral summer off the coast of Tasmania.

In the absence of continental influence (e.g. biomass burning and anthropogenic sources), SO aerosol is composed of particles associated with ocean biology and, near the ocean surface, sea spray. Aerosols fall into four modes: coarse (diameters > 1 μm), accumulation (0.1-1 μm), Aitken (0.01-0.1 μm) and nucleation (<0.01 μm) (Bates, 2002; Clarke et al., 1998; Seinfeld & Pandis, 2016). Collectively, aerosols from all modes taken together are referred to as condensation nuclei (CN). Accumulation mode aerosols are the main contributors to cloud condensation nuclei (CCN) and are of central importance to ACI through their control of cloud droplet number (N_d) and overall cloud albedo (Twomey, 1977). The role of giant CCN (≥ 2 μm) (Jensen & Nugent, 2017) sampled during SOCRATES (McFarquhar et al., 2020) on SO precipitation will be the topic of future papers. The number concentration of particles in the SO is dominated by Aitken mode and small accumulation mode particles while the mass is dominated by coarse mode particles (Ayers et al., 1997). Sea spray production mechanisms contribute larger accumulation mode and coarse mode particles (diameters ≥ 0.2 μm) (Bigg & Leck, 2008; Fitzgerald, 1991; Grythe et al., 2014; Quinn et al., 2017) and dominate the wintertime marine boundary layer (MBL) when biogenic sources are inactive. However, sea spray aerosol is not the major contributor to summertime CCN (Modini et al., 2015; Prather et al., 2013; Quinn et al., 2015) as these particles are estimated to contribute less than 30% of CCN between 70°S and 80°N (Quinn et al., 2017).

Phytoplankton significantly influences the aerosol budget over the SO and other remote marine regions during biologically active periods (e.g. spring and summer). Dimethylsulfonium propionate (DMSP) is emitted by phytoplankton and subsequently cleaved into dimethyl sulfide (DMS) and fluxed into the atmosphere. DMS oxidizes into methane sulfonic acid (MSA) and sulfur dioxide (SO_2), which can further oxidize into sulfuric acid (H_2SO_4) (Ayers et al., 1997; Fitzgerald, 1991; Quinn & Bates, 2011; Seinfeld & Pandis, 2016). SO_2 can also react in cloud droplets through aqueous-phase oxidation and, after drop evaporation, create non-sea-salt sulfate (nss-SO_4) particles which are extremely effective CCN (Charlson et al., 1987; Hobbs, 1971). CCN also grow from coagulation of smaller Aitken or accumulation mode particles (Seinfeld & Pandis, 2016) and from vapor deposition of DMS oxidation products (Ayers et al., 1997; Ayers & Gillett, 2000; Ayers & Gras, 1991; Bates et al., 1998; Charlson et al., 1987) or organic gases (Zheng et al., 2020) onto existing particles.

Aitken particles form mainly through homogeneous nucleation of precursor gases (Seinfeld & Pandis, 2016), which, in the SO and other marine environments, are predominantly H_2SO_4 and MSA (Ayers et al., 1997; Fitzgerald, 1991). Ions, organics, and other compounds can also play a role in particle formation (Dunne et al., 2016; Gordon et al., 2017; Kerminen et al., 2018). For gas to particle conversion to occur, precursor gases must be present and the total aerosol surface area (SA, driven by coarse and accumulation mode sizes) must be low enough to discourage vapor deposition on to preexisting particles (≤ ~10 μg cm^{-3}) (Clarke et al., 1998; Covert et al., 1996). This low SA is likely to occur in the SO free troposphere (FT) (Clarke, 1993).

The majority of Aitken mode particles in marine regions are produced through gas to particle conversion of DMS oxidation products in the FT and, after entraining or subsiding into and growing in the MBL, they are the key source of CCN in the summertime SO. CCN (roughly

diameters ≤ 0.2 μm) in the SO (Bigg, 2007; Bigg & Leck, 2008; Quinn et al., 2017), and generally in remote marine environments between 70°S and 80°N (Quinn et al., 2017), are dominated by nss-SO_4 in biologically active periods. These particles are often associated with large scale meteorology that causes entrainment of recently formed Aitken particles from the FT into the MBL (Quinn et al., 2017), which is thought to be the main source of aerosol number in marine regions at low and middle latitudes (Kerminen et al., 2018). Variability in SO aerosol concentrations is associated with frontal passages, rapidly bringing Aitken and nucleation mode particles into the MBL from the FT (40-70°S) (Bates et al., 1998; Covert et al., 1996). These particles grow into CCN through gas condensation (Ayers et al., 1997; Ayers & Gillett, 2000; Ayers & Gras, 1991; Bates et al., 1998; Charlson et al., 1987) and cloud processing (Sanchez et al., 2021; Schmale et al., 2019), dominating aerosol size distributions between 20-70°S (Covert et al., 1996). Similar behavior is seen in the stormy, biologically active north Atlantic (Sanchez et al., 2018; Zheng et al., 2020; Zheng et al., 2018). Faster descent over the SO relative to the tropics reduces the amount of coagulation and growth that occurs (Clarke et al., 1998), which, along with MBL residence time (Covert et al., 1996), affects how many aerosols grow to CCN sizes.

Lack of positive correlations between aerosol surface area (SA) and concentrations of nucleation mode particles in the SO MBL (Covert et al., 1996) suggest that new particle formation is uncommon in the MBL (Bates et al., 1998) but instead occurs in the FT and subsides into the MBL (Humphries et al., 2016; Sanchez et al., 2021; Schmale et al., 2019; Williamson et al., 2019). This is consistent with the idea that short-term variability in MBL CCN and CN is both limited and tied to FT processes (Raes, 1995). A global chemical transport model estimation finds 43-65% of zonal mean CCN over the southern hemisphere summertime oceans are from FT nucleated sulfate entrained and grown in the MBL (the dominant microphysical pathway for DMS influencing southern hemisphere marine CCN) (Korhonen et al., 2008). More recent modeling efforts have found the majority of spatiotemporal patterns in SO N_d are explained by nss-SO_4 (35-45°S) and organic matter in sea spray (45-55°S), increasing the mean summertime reflected shortwave by more than 10 W m^{-2} (D. T. McCoy et al., 2015).

Previously observed FT particle production over the SO has been associated with cloud outflow (Clarke et al., 1998; Weber et al., 2001), a dominant particle formation mechanism throughout the world that can involve a variety of cloud types (Kerminen et al., 2018) and substantially influence aerosol concentrations (Twohy et al., 2002). Particle formation associated with low cumulus clouds (Clarke et al., 1998) and a frontal cloud system (Weber et al., 2001) have been observed over the SO simultaneous with H_2SO_4 vapors. Details have yet to be quantified (Kerminen et al., 2018), but cloud outflow production broadly involves air masses rich in precursor gases brought up through cloud and cleansed of accumulation and coarse mode aerosol (reducing SA) through cloud droplet scavenging and precipitation processes.

After exiting cloud, precursor gases can oxidize and undergo gas to particle conversion (low SA means pre-existing aerosols cannot scavenge these vapors (Weber et al., 2001)). Depending on the exposure to liquid water, less water-soluble gases (e.g. DMS (Seinfeld & Pandis, 2016)) better survive cloud and precipitation processing. Large eddy scale simulations of gases processing through cloud before particle formation in cumulus outflow in the south east Pacific (Kazil et al., 2011) suggest DMS is likely lofted through clouds before oxidizing into precursor gases (e.g. MSA, SO_2 then H_2SO_4) after exposure to OH upon cloud exit.

Environments at higher altitudes over the SO are conducive to particle formation (Weber et al., 2001): i) increased actinic flux from heightened upwelling and downwelling radiation

combined with heightened water vapor concentrations in cloud outflows can lead to increases in OH and subsequent oxidation of DMS and its products, increasing precursor gas concentrations, and ii) colder temperatures aloft increase the supersaturation of precursor gas concentrations, increasing nucleation rates (Kirkby et al., 2011). Particle production rates at these altitudes are incompletely explained by binary reactions (i.e. H_2SO_4-H_2O) (Weber et al., 2001) suggesting other factors may also be involved (e.g. organics, ammonia, ions, etc.) (Dunne et al., 2016; Gordon et al., 2017; Kirkby et al., 2011; Kürten et al., 2016).

SOCRATES was designed to expand our knowledge of the sources and sinks of aerosol and the ACI in SO cyclone cold sectors (45-62°S), a regime where Aitken aerosols are abundant in the MBL (Covert et al., 1996; Quinn et al., 2017) and new particle formation occurs aloft (Clarke et al., 1998; Weber et al., 2001). We detail widespread observations of recent particle formation in the FT (3- 6 km) and the synoptic uplift mechanism that explains these frequently occurring events (Section 3.1). Patterns of cloud, aerosol, and the resulting ACI are examined and, building on earlier aerosol life-cycle and variability studies (Quinn et al., 2017; Raes, 1995), a mechanism is hypothesized for N_d maintenance in SO clouds and pristine environments due to entrained Aitken aerosol influence (Section 3.2). Global weather and climate models (GCMs) simulate insufficiently bright low clouds in SO cold sectors (Bodas-Salcedo et al., 2016; Bodas-Salcedo et al., 2012; Bodas-Salcedo et al., 2014; Williams et al., 2013), either due to excessive glaciation of mixed-phase clouds or biases in CCN, N_d, and ACI (Bodas-Salcedo et al., 2019; I. L. McCoy et al., 2020; Revell et al., 2019). Observational comparisons with SOCRATES nudged GCMs highlight systematic biases that will help disentangle the cause of this radiative bias (Section 3.3). We begin by describing our methodology, datasets, and models (Section 2) and conclude with a discussion of the implications of this analysis and future steps (Section 4) as well as a summary of our results (Section 5).

2 Materials and Methods

2.1 Aircraft Sampling

In the SOCRATES campaign (McFarquhar et al., 2020), the National Science Foundation Gulfstream-V (GV) aircraft flew out of Hobart, Tasmania, over the SO. Fifteen flights (Figure S1) were designed to sample low clouds in the cold sectors of cyclones. Each research flight (RF) had a similar sampling strategy (Figure 1). The GV flew a high (~6 km altitude) survey leg in the mid-troposphere (MT) into a region forecast to be dominated by low clouds, descending after a southernmost latitude was reached (~60-62°S). After descending to an altitude above cloud (~3 km), the GV returned to Hobart conducting repeated MBL flight modules. Each module consisted of 10-minute level legs above cloud (AC), in cloud (IC), and sub cloud (SC) at 150 m above the sea surface, followed by sawtooth profiling through the MBL (Figure 1). Module sampling was continued as long as operational constraints allowed after which the plane climbed back above the MBL to return to Hobart. There were two exceptions to this method during the campaign: RF11 and 15 had flight paths customized for targeting cumulus cloud tops to sample mixed-phase microphysics. The limited observations obtained north of 45°S are affected by proximity to Australia. Thus, our analysis focuses on the SO sampled between 45 and 62°S.

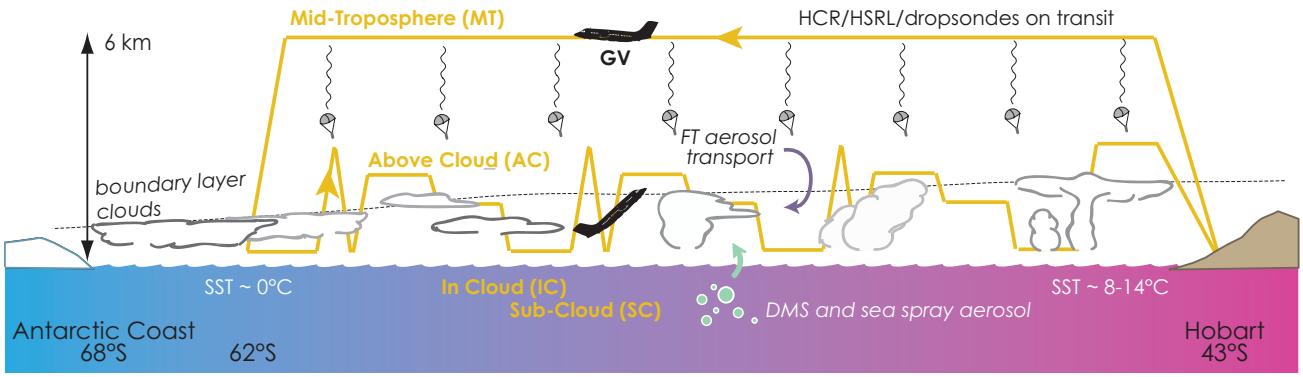

Figure 1 Standard flight module for SOCRATES with identified sampling regions: mid-troposphere (MT), above cloud (AC), in cloud (IC), and sub-cloud (SC). A cloud radar (HCR), lidar (HSRL), and dropsondes were used to probe the underlying cloudy MBL on MT survey legs but are not explicitly utilized in this analysis (McFarquhar et al., 2020).

The GV was equipped with a wide array of instruments (McFarquhar et al., 2020). The low-rate, 1 Hz flight, state, and microphysical data from the GV were used in this analysis (UCAR/NCAR, 2019). The cloud droplet number concentration (N_d) is from the cloud droplet probe (CDP). Aerosol number concentrations used in our analysis are taken from two instruments: a condensation nuclei counter (CN, aerosol diameters ≥ 0.011 μm) and an ultra-high sensitivity aerosol spectrometer (UHSAS). Respectively, the instrument models used were a TSI-3760A condensation nucleus counter on a HIAPER modular inlet and a DMT UHSAS-A, S/N 001. The UHSAS provides both size-resolved and integrated concentrations. The smallest size bins (diameters < 0.1 μm) are neglected due to sizing difficulties. Accumulation mode number concentrations are reported as UHSAS100 (0.1 – 1 μm diameter) throughout the paper, consistent with the expected size range for this mode. Size resolved number concentrations for coarse mode aerosol are from the CDP (2 – 50 μm diameter).

The surface area (SA) reported in this paper is computed from the coarse and accumulation mode size distributions (diameters between 0.1 and 50 μm). UHSAS reports essentially dry aerosol diameters except for the largest particles (Sanchez et al., 2021) while the CDP retains ambient diameters. Accumulation mode SA is adjusted for swelling associated with the environmental relative humidity before it is added to the coarse mode SA from the CDP. We use the growth factor reported for extinction coefficients, f_{grow}, in eq. 3 of Chand et al. (2012) scaled by 2/3 to account for SA growth (*personal communication Mike Reeves, NCAR*):

$$SA_{UHSAS} = \pi D_{UHSAS}^2 f_{grow}^{2/3} \quad (1)$$

As in Chand et al. (2012), the values assumed in calculating f_{grow} are for sulfate aerosols, a somewhat smaller growth factor than for sea salt aerosols. This is a reasonable assumption because sulfate or sulfur-based aerosols were the most frequently observed throughout the campaign (Section 3.1.3).

All aerosol measurements are subject to screening by a cloud and rain mask based on the CDP and the two-dimensional optical array probe (2D-C). Aerosol observations were discarded when our empirically chosen thresholds were exceeded: liquid water content from the CDP ≥ 0.001 g m^{-3} or precipitation droplets from the 2D-C ≥ 0.1 L^{-1}. Samples were removed for 10 seconds following detection of cloud or drizzle to avoid measurement contamination. Measured temperature and pressure are used to adjust aerosol concentrations to mg^{-1} from cm^{-3} to account

for volume changes at different levels in the atmosphere. Note that concentrations of mg^{-1} can be converted to "cm^{-3} at STP" by a factor of 1.25. Cumulative size distributions are calculated from drizzle and cloud-screened aerosol number concentrations for CN, size resolved UHSAS, and size resolved CDP.

Aerosol measurements behind a counterflow virtual impactor (CVI) (Noone et al., 1988; Twohy et al., 1997) are used to interpret aerosol composition in two ways. First, Twohy et al. (2021) use a scanning transmission electron microscope (STEM) and X-ray analysis of particles impacted on formvar carbon grids for examining particles (diameters 0.1-1 μm) AC, IC, and SC (Twohy et al., 2013). Specific examples for particles with diameters 0.1-0.5 μm are highlighted here, see Twohy et al. (2021) for complete examination. Second, particle volatility estimates are reconstructed for FT particles from comparing CVI heated CN (using a TSI-3010 condensation nucleus counter, CN_{CVI}) and UHSAS100 (using a UHSAS-G, S/N 15 as in Kupc et al. (2018), $UHSAS100_{CVI}$) measurements to un-heated CN and UHSAS100 measurements. Specifics of the CVI set up for SOCRATES that allowed for this volatility analysis are detailed in supplementary text S1. Particles are considered "volatilized" in this arrangement when their diameter is reduced to below the detection limit for CN_{CVI} (0.011 μm) or $UHSAS100_{CVI}$ (0.1 μm) but they are likely not completely evaporated.

Observations from the 2015 Cloud System Evolution in the Trades (CSET) campaign (Albrecht et al., 2019) in the north east Pacific (NEP) provide a subtropical comparison for SOCRATES. This comparison is modeled after Clarke et al. (1998) who used a similar tropical comparison to establish the uniqueness of the SO. CSET sampled the stratocumulus to trade cumulus transition between California and Hawaii using a modular strategy similar to SOCRATES. Observations east of 130°W are continentally influenced and thus excluded from this analysis. The GV during CSET was equipped with comparable wing-mounted instrumentation including the CN, UHSAS, CDP, and 2D-C (UCAR/NCAR, 2017). The same data screening and analysis methodology is applied to both campaigns.

Two kinds of binning composite methods are used in this paper. The first is a temporal by altitude composite where median values are computed for observations from each flight binned by 2 min in duration and 50 m in altitude. This is used for the majority of comparisons including N_d versus UHSAS100 matches for interpreting ACI. The second is a distance by altitude composite for describing regional characteristics. CSET and SOCRATES flight paths approximately fall along common distance axes: a diagonal line between the coast of California and Hawaii (CSET) (Bretherton et al., 2019) and a roughly north-south line between Hobart, Tasmania and the coast of Antarctica (SOCRATES) (Figure S1). Median values are computed in 500 m altitude layers and 1.5° along the appropriate axis. Only bins with at least ten 1 Hz flight observations are considered for both composite methods and aerosol samples are subject to the same precipitation and cloud screening as described above. Individual distance by altitude flight composites are averaged together to develop a mean campaign composite as in Bretherton et al. (2019). Note that all correlation coefficients and *p*-values in this study are for Pearson correlations, significance is assumed at 95% confidence, and R^2 is the variance explained.

2.2 Air-mass Back Trajectories

Interpreting SOCRATES aerosol observations requires knowledge of their air mass histories. The Hybrid Single Particle Lagrangian Integrated Trajectory (HYSPLIT) model (Stein et al., 2015) helps to provide this context. HYSPLIT back trajectories were based on Global Data Assimilation System (GDAS) meteorology on a 0.5° by 0.5° grid. Seventy-two hour back-

trajectories were calculated for each 10-minute flight segment initialized with the aircraft altitude, latitude, and longitude at the mean segment time.

2.3 Nudged Global Climate Model Simulations

A goal of both SOCRATES and CSET was to use observations to evaluate the fidelity of current GCMs. One method is to compare campaign observations with reanalysis-nudged hindcasts from GCMs, as in Bretherton et al. (2019). This approach is applied to evaluate version 6 of the Community Atmosphere Model (CAM6), which uses the MAM4 aerosol scheme detailed in Liu et al. (2016). CAM6 SOCRATES simulations and microphysics are described in detail by Gettelman et al. (2020). CAM6 is nudged by wind, temperature, and surface pressure fields from MERRA2 reanalysis (Gelaro et al., 2017) with a 1-day relaxation timescale. This ensures the large-scale structure of simulated storms are close to the reanalysis, enabling simulation of similar profiles of clouds, humidity, and aerosols in the model when compared to aircraft observations at a given location and time. Clouds, humidity, and aerosols are not nudged in CAM6, allowing a critical appraisal of their accuracy using the GV measurements. Model data are co-located to observations by linearly interpolating to temporal and spatial locations from the 2 min x 50 m observational composites (Section 2.1) for CSET and SOCRATES.

We focus on comparing the observed aerosol and N_d concentrations with CAM6. CAM6 in-cloud N_d is computed as N_d divided by liquid cloud fraction (when cloud fraction ≤ 10%, we set N_d=0). CAM6 aerosol number concentrations are computed using a bounded log-normal distribution (Zender, 2001) for each of the instrument specified diameter ranges (D_{min} to D_{max}):

$$N(D_{min}, D_{max}) = \frac{N_0}{2}\left[erf\left(\frac{ln(D_{max}/D_m)}{\sqrt{2}\,ln(\sigma_m)}\right) - erf\left(\frac{ln(D_{min}/D_m)}{\sqrt{2}\,ln(\sigma_m)}\right)\right} \quad (2)$$

where σ_m is the modal width parameter, D_m is the modal diameter, and N_0 is the modal number concentration for each of the four modes in MAM4. The modal width parameter is 1.6 for accumulation, Aitken, and primary carbon modes and 1.2 for the coarse mode. The modal number contribution for both interstitial and out-of-cloud aerosol in the specified diameter range is calculated using (2). The individual mode contributions are summed to produce the total, instrumentally-matched CAM6 number concentration. These values can be directly compared with observations because both count the number of particles within a specified size range.

Two instrumentally-matched values are calculated using the bounded log-normal: CN (0.011 – 30 μm) and UHSAS100 (0.1 – 1 μm). Results using this model-derived UHSAS100 are similar to CAM6 CCN concentrations at a supersaturation of 0.2% for SOCRATES (CCN at 0.2% (Sanchez & Roberts, 2018) is the closest proxy for UHSAS100 observationally, Figure S2). However, CCN was not measured during CSET so no comparable relationship can be deduced. The more complex but exact method of using a bounded log-normal distribution for comparing modeled and observed aerosol number concentrations is thus necessary.

3 Results

3.1 Synoptically Generated Recent Particle Formation

3.1.1 Observations of Recent Particle Formation in the Southern Ocean and Sub-Tropics

Evidence of recently formed particles occurring in the SO FT was observed frequently during SOCRATES. Two example flight segments (Figure 2) have been selected to show the simultaneously-occurring signatures that suggested recent particle formation: a MT survey leg

(Figure 2a, ~6 km altitude, 1200 km long) and an AC leg (Figure 2b, ~3 km altitude, 300 km long). The first characteristic is large CN concentrations (≥ 1000 mg^{-1} and often exceeding 2500 mg^{-1}), which often varied rapidly (up to tenfold changes in concentration over a few km). CN variability possibly marks recent bursts of particle formation or boundaries between different air masses at different stages of nucleation (Clement et al., 2002). The second notable characteristic is anti-correlation between UHSAS100 and CN concentrations (Covert et al., 1996) (i.e. low UHSAS100 occurring with high CN). Finally, SA estimated from coarse and accumulation mode particles is below the threshold enabling new particle formation ($SA \leq 10$ μm^2 mg^{-1}) (Clarke et al., 1998; Covert et al., 1996).

Based on these signatures of recent particle formation, we use the maximum CN concentration for a 10-minute flight segment (CN_{Max10}) to identify likely recent particle formation (RPF) events in this pristine environment. We find that the upper quartile of CN_{Max10} across the campaign ($CN_{Max10} \geq 2500$ mg^{-1}) captures the majority of RPF cases observed. We define the lower three quartiles ($CN_{Max10} < 2500$ mg^{-1}) as unclear or non-RPF cases. This restrictive methodology allows us to be confident in identifying RPF events for statistical analysis of associated air mass histories and driving mechanisms (see Section 3.1.2). Instances of $CN \geq 1000$ mg^{-1} are likely also associated with RPF but may be more aged (e.g. older, coagulated Aitken particles) and have less distinct air mass histories. RPF identified by the CN_{Max10} criteria are indicated in Figure 2 and corresponding air mass trajectories can be seen in Figure S3.

Clement et al. (2002) found that recently formed sulfuric acid particles in the upper troposphere grew to observable sizes (~0.0125- 0.03 μm, comparable to our CN observation limit of 0.011 μm) within ~5-10 hours. While their analysis used different instrumentation and occurred in the outflow of a mid-latitude storm system, this estimate is useful for interpreting timescales of particle growth during SOCRATES. Based on this, recently formed particles observed during SOCRATES are assumed to be within at least 5-10 hours of new particle formation though may be more aged.

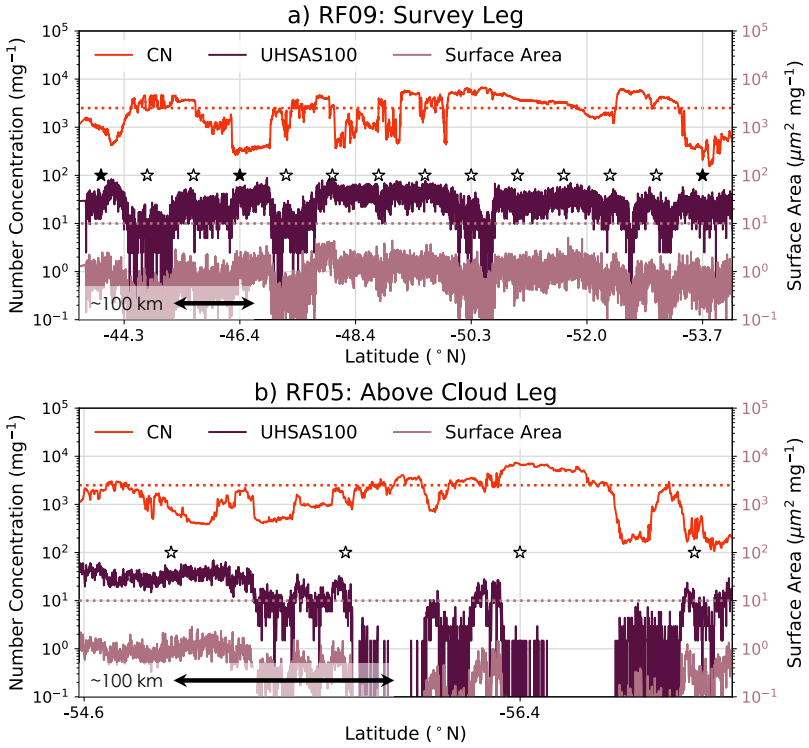

Figure 2 Example cases for suspected recent particle formation events observed in (a) survey-leg sampling in the mid-troposphere during RF09, and (b) above-cloud leg sampling during RF05. Observations are shown against time as flight proceeded south (note difference in length scale between a and b). Number concentrations (left axis) for total (CN, orange) and accumulation mode (UHSAS100, purple) particles. Surface area for coarse and accumulation mode aerosol (right axis, pink). Dotted lines for 2500 mg^{-1} (orange) and 10 μm^2 mg^{-1} (pink) are included for reference. HYSPLIT trajectory initial locations are marked, solid stars for non-RPF events (CN_{Max10}<2500 mg^{-1}) and open stars for RPF events (CN_{Max10}>2500 mg^{-1}). Corresponding HYSPLIT trajectory ascent profiles are shown in Figure S3.

The SO FT is dominated by small aerosol particles (diameters < 0.1 µm) (Figure 3, orange). All SOCRATES flight data for CN and UHSAS100 is split by altitude, screened for cloud and drizzle, and used to compute normalized pdfs for three altitude segments (following regions defined in Figure 1): mid-troposphere (MT: Z ≥ 4.5 km, a and b), above-cloud (AC: 1.5 ≤ Z ≤ 4.5 km, c and d), and sub-cloud (SC: Z ≤ 1.5 km, e and f). In both the MT and AC sampling, a significant percentage (~25%) of SOCRATES samples have CN ≥ 1000 mg^{-1} (Figure 3b, d). These large FT CN concentrations are due to the prevalence of Aitken mode particles since the UHSAS100 pdfs at these levels rarely exceed 100 mg^{-1} (<1%, Figure 3a, c).

Concentrations of CN ≥ 2500 mg^{-1} are less frequent in the sub-cloud layer (<1% compared to ~15% in the FT), suggesting MBL new particle formation is rare. However, Aitken aerosol particles are prominent in the MBL: the SC CN pdf retains significant probability near 1000 mg^{-1} (~15%) while SC UHSAS100 concentrations greater than 200 mg^{-1} are rare (~5%) (Figure 3e, f). UHSAS100 pdfs exhibit a small shift to higher frequencies with decreasing altitude between MT and AC (from ~25 to ~35 mg^{-1} in the median) and a larger shift between AC and SC (~35 to ~60 mg^{-1} in the median) indicating some coagulation and growth is occurring as particles descend. The larger AC-SC change is consistent with cloud processing and condensational growth within the MBL being important for increasing accumulation mode concentrations.

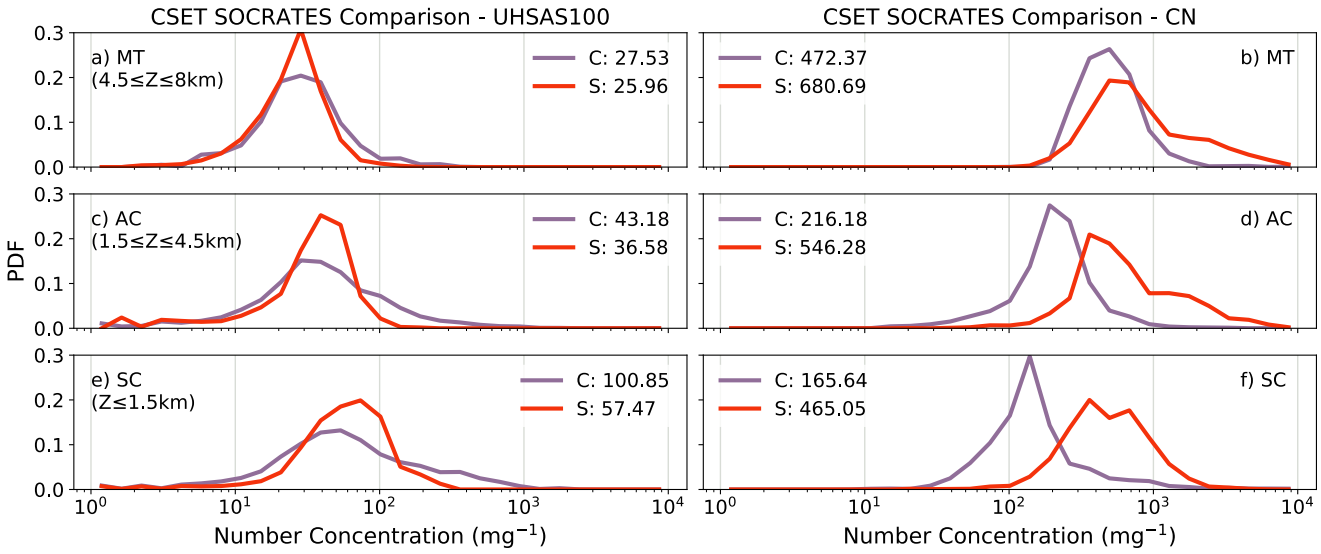

Figure 3 Pdfs of number concentrations for UHSAS100 (a, c, e) and CN (b, d, f) for different altitudes: mid-troposphere (a, b), above cloud (c, d), and sub-cloud (e, f). Altitudes used for each range are listed in a, c, and e. SOCRATES observations (S, orange) are contrasted with CSET observations (C, purple). Median values are included for comparison.

To determine the uniqueness of the SO aerosol vertical structure and distribution, we contrast the height-matched SOCRATES number concentration pdfs with comparable pdfs in a typical sub-tropical environment sampled during CSET (Figure 3, purple). At all altitude levels, subtropical UHSAS100 occurs both for a wider range of concentrations and more frequently at high concentrations compared to SO observations (Figure 3a, c, e). Lower and less variable CN concentrations typify CSET compared to SOCRATES, indicating lower Aitken mode concentrations in the subtropics than over the SO. However, regional differences in Aitken mode concentrations vary vertically: SC CN pdfs are the most separated (Figure 3f) while MT CN pdfs are the most similar (Figure 3b) between campaigns.

These results have several implications for SO aerosol sources. If local, wind-driven sea-spray production was responsible for driving MBL aerosol number production in the SO, we would expect a higher ratio of UHSAS100 to CN concentrations in SOCRATES where winds are stronger compared to CSET (means of 14 vs. 7 m s^{-1} within 200 m of the surface). This is opposite the observed behavior (Figure 3e, f), signaling that primary aerosol production is not the largest contributor to CN in the SO. While CN number concentration may not be driven by sea spray production, increased surface gas emissions associated with higher wind speeds (Lana et al., 2011) may still assist in secondary aerosol production and in growing aerosols in the SO.

Sub-tropical aerosols sampled in CSET were, in general, more aged than SO aerosols sampled in SOCRATES. CSET observations at 6 km typically had a low relative humidity (mean ~15 vs. ~30% during comparable SO sampling), implying a height of last saturation in the sub-tropics between 9-10 km. This is consistent with outflow from deep convective clouds, which can generate particles that subsequently coagulate as they slowly descend through the atmosphere (Clarke et al., 1998; Williamson et al., 2019). MT CN concentrations exceeding 1000 mg^{-1} occur less frequently during CSET than SOCRATES (~10% vs. ~30%) while MT UHSAS100 exceeding 100 mg^{-1} occur occasionally (~2% vs. none), consistent with sampling

more aged aerosols in the sub-tropics which have descended from nucleation events above 6 km (Figure 3a, b). There are no instances of MT or AC CN ≥ 2500 mg^{-1} during CSET (Figure 3b, d), indicating SO aerosol is more recently formed and sub-tropical RPF is rare at these altitudes. Continued aging with descent explains the rare occurrence of CN ≥ 1000 mg^{-1} AC and SC in CSET compared to SOCRATES (none vs. ~25% AC, <1% vs. ~15% SC, Figure 3d, f). Coagulation and growth processes are also more active in the sub-tropics than the SO, consistent with Clarke et al. (1998): during CSET compared to SOCRATES, UHSAS100 pdfs shift with descent to larger concentrations (~25 to ~45 to ~100 vs. ~25 to ~35 to ~55 mg^{-1} in the median), CN to smaller (~470 to ~215 to ~165 vs. ~680 to ~550 to ~465 mg^{-1} in the median) (Figure 3c, d to e, f).

3.1.2 Evidence for Particle Generation through Synoptic Uplift Mechanism

Remarkably high concentrations of Aitken mode aerosol particles frequently occur in the lower SO FT. Preceding studies (Section 1, e.g. Clarke et al. (1998), Weber et al. (2001)) have identified multiple forms of cloud outflow particle production mechanisms taking place over the SO. However, these mechanisms do not fully explain the quantity or location of RPF observed in the AC and MT layers during SOCRATES (Figure 3d, b). Clarke et al. (1998) identified new particle formation in outflow from cumulus congestus rising above the mean SO MBL. SOCRATES sampled infrequently in or downwind of such regimes. Weber et al. (2001) observed new particles and sulfuric acid vapors in the outflow of a frontal system off of Tasmania at ~6 km. SOCRATES observed RPF near a similar frontal system but not all MT events were associated with this type of feature. New particles have been observed in outflow regions of deep convection in the subtropics and mid-latitudes (Kerminen et al., 2018) which, along with frontal systems and general convective vertical motion, Covert et al. (1996) hypothesized were essential in generating FT Aitken particles. However, high concentrations of Aitken particles and RPF were observed on most SOCRATES flights and across a range of weather regimes with little evidence of recent penetrative congestus convection upstream.

SOCRATES provides the first opportunity to statistically analyze SO RPF events and holistically understand the particle production mechanisms generating them. Based on the frequent detection of RPF across varied weather regimes and altitudes during SOCRATES, and building on these earlier studies, we hypothesize that synoptic scale motions routinely generate new particles in the summertime SO FT. New particles are formed and dispersed after boundary-layer air is lifted and processed through precipitating clouds forming in regions of synoptic scale ascent. Two vital steps for gas to particle formation (Section 1) occur during synoptic-uplift: i) aerosol SA in the air mass is reduced during uplift through collision-coalescence processes associated with clouds and precipitation, and ii) DMS (and/or DMS-oxidation products) is lofted from the surface to an environment where it can oxidize, undergo photochemical reactions, and nucleate into new particles instead of depositing onto pre-existing aerosol particles (Covert et al., 1996; Kerminen et al., 2018; Seinfeld & Pandis, 2016; Weber et al., 2001).

We test this synoptic uplift mechanism by examining the altitude history of the MT air masses sampled in SOCRATES using RPF and non-RPF identified HYSPLIT 72-hour back trajectories (Figure 4a, b) (Section 2.2). RPF air masses exhibit a much steeper composite ascent profile over the past 72-hours compared to the non-RPF composite profile (Figure 4a). During the ascent period (10 to 70 hours back), the mean ascent rate for the RPF cases (1.1 cm s^{-1}) is comparable with estimates of the characteristic vertical velocity in mid-latitude synoptic systems (~1 cm s^{-1}) (Holton & Haikm, 2013). The non-RPF cases have significantly slower mean ascent

rates (0.6 cm s^{-1}). The deep uplift of the RPF air masses presumably creates thick precipitating clouds, which process and remove accumulation and coarse mode aerosols. RPF cases also originate from below 1 km more frequently in the proceeding 72 hours compared to non-RPF cases (Figure 4b). Thus, RPF trajectories have the opportunity to source the necessary precursor gases (e.g. DMS) from the boundary-layer, which is necessary for gas to particle conversion to take place.

AC RPF events are similarly examined (Figure 4c, d). There is a clear distinction between the RPF and non-RPF cases in the 48 hours prior to sampling: the RPF case composite shown in Figure 4c has a rapid synoptic ascent profile (1 cm s^{-1} in the last 20 hours) and most RPF back-trajectories come from below 1 km (Figure 4d). On average, the non-RPF trajectories show zero mean ascent over the previous 72 hours.

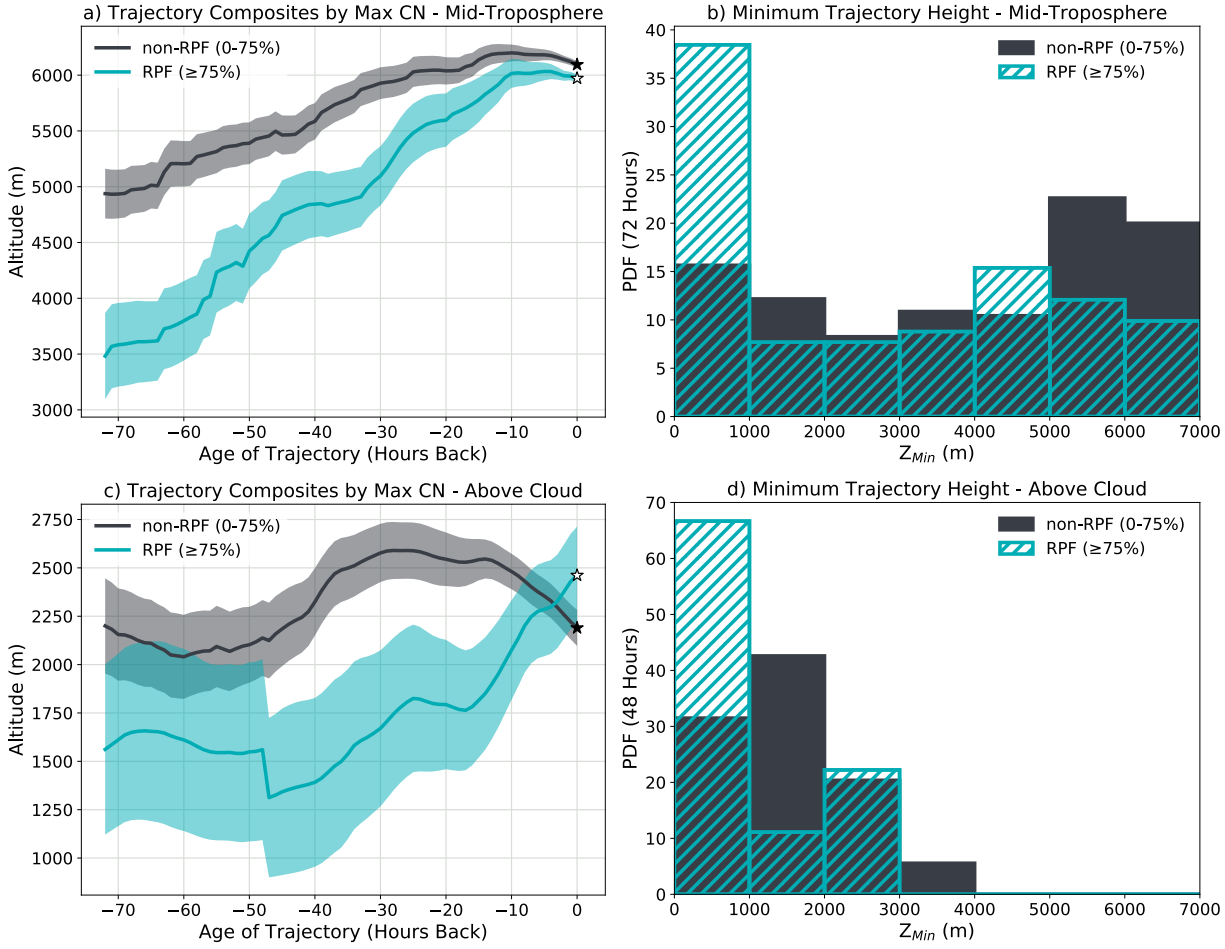

Figure 4 Mean (line) and its corresponding standard error (shading) of ascent profiles for HYSPLIT trajectories initiated in the mid-troposphere (a) and above cloud (c). Corresponding distributions of minimum height over preceding time where altitude profiles are statistically distinct: 72-hours for mid-troposphere (b) and 48-hours for above cloud (d). Trajectories are composited by CN_{Max10} into RPF events (blue, $CN_{Max10} \geq 75^{th}$ percentile) and non-RPF events (gray, $CN_{Max10} < 75^{th}$ percentile). Number of RPF vs non-RPF cases per SOCRATES research flight for mid-troposphere and above-cloud are shown in Figure S4.

We use ECMWF ERA5 reanalysis to investigate the large-scale synoptic patterns driving the uplift associated with SO RPF. Flight RF07 is used as an example to demonstrate the typical synoptic patterns responsible for RPF events, as many RPF identified back-trajectories occurred during its survey leg (~6 km) (Figure 5). Rapid ascent from the MBL on these back-trajectories

occurred in two periods: ~60 hours (Figure 5a, b) and ~36 hours (Figure 5a, c) prior to GV sampling. Vertical velocity and geopotential height fields at 700 hPa (chosen as a representative mid-level altitude) help to identify the cause of this uplift: a warm conveyor belt (WCB). The WCB moves along an eastward propagating Rossby wave (traced by a representative geopotential height contour in Figure 5b, c). At ~60 hours (Figure 5b), a tongue of warm, moist MBL air from the sub-tropics is advected up towards the mid-troposphere and poleward ahead of the cold front (42°S, 54°E). At ~36 hours (Figure 5c), trajectories off the edge of Antarctica (60°S, 100°E) undergo uplift associated with the remains of the WCB that has traveled along the Rossby wave. The WCB generates potential vorticity anomalies that drive the upward motion responsible for RPF. Sub-polar vortices (e.g. 60°S, 70°E and 54°S, 140°E, Figure 5c) led to uplift of MBL air to the MT in other research flight cases but did not affect the trajectories sampled during RF07.

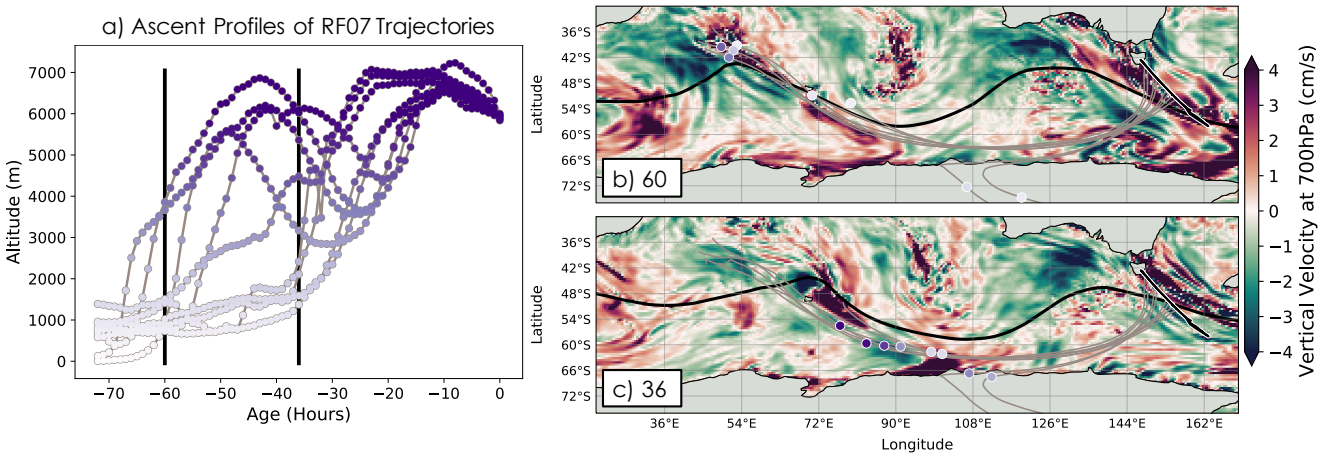

Figure 5 Illustration of synoptic scale patterns influencing MT RPF identified air masses sampled by RF07 (black line from Tasmania, b and c). Two times of uplift are of note (ascent marked by black lines in a): 60 (b) and 36 (c) hours prior to GV sampling. ERA5 reanalysis maps at these times of interest include 700 hPa vertical velocity (colors) with a reference 700 hPa geopotential height contour at 2.9 km (black contour). The geopotential height contour separates warmer, moister sub-tropical air from cooler, drier polar air and marks the Rossby wave propagating to the East. RPF trajectories (gray lines) with air mass locations (circles) colored by their altitude (white to purple, as in the ascent profiles in a). Ascent of the first set of trajectories at 60-hr (b) occurs off the tip of Africa while ascent of the 36-hr trajectories (c) occurs off the coast of Antarctica, both driven by the advance of a warm-conveyor belt towards the south east (i.e. along the height contour and Rossby wave). Note sub-polar vortices affecting the vertical velocity in c) at 60°S, 72°E and 54°S, 140° E. An animation of the RF07 synoptic event is included in supplemental material, MS01.

Synoptic analysis of all SOCRATES flights reveals that uplift along RPF trajectories is typically associated with either warm conveyor belts or sub-polar vortices. The particle production observed in cloud outflow from a frontal system by Weber et al. (2001) would be considered a WCB example of the synoptic-uplift mechanism. In the southern hemisphere, WCBs are not always associated with cyclones and occur frequently off the tip of South America and South Africa (Catto et al., 2015). WCBs are also not as constrained in longitude in the southern hemisphere as in the northern hemisphere, occurring frequently across a wide range of longitudes in the SO (Eckhardt et al., 2004). The behavior of MT RPF back trajectories is consistent with both these characteristics of WCB behavior in the SO: i) the typical RPF trajectory path arcs down from South Africa towards Antarctica, funneling along the large-scale waves in the region, and ii) the geographic location of minimum RPF trajectory altitudes is widespread across the SO (Figure S5).

Widespread and frequent RPF occurrence across the summertime SO free troposphere is ensured due to the regularity of synoptic uplift (i.e. aerosol cleansing and lofting of air masses to favorable environments for gas to particle formation) and ubiquitous, DMS-rich boundary-layer air (i.e. air masses enriched in precursor gases, ensured by many regions with significant DMS fluxes in the austral summer (Lana et al., 2011)). The synoptic-uplift mechanism (Figure 6) works together with other particle formation mechanisms in the region (Clarke et al., 1998) to create a free troposphere that is frequently rich in Aitken particles. This has a profound impact on N_d and ACI in the SO, as will be discussed in Section 3.2.

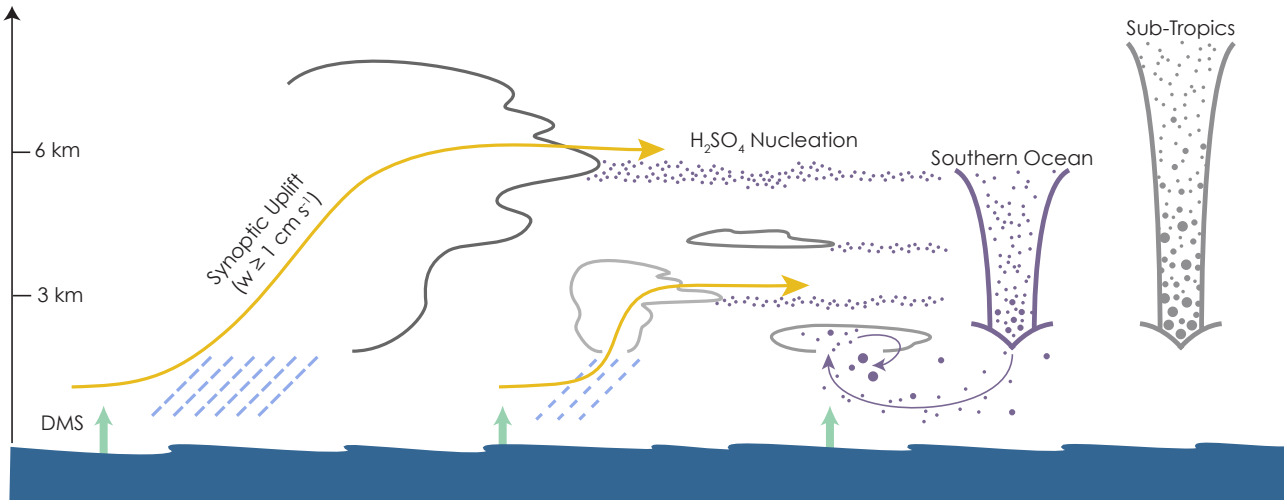

Figure 6 Diagram of aerosol generation and cycling associated with the novel synoptic uplift mechanism for new particle formation. Yellow arrows signify synoptic motions (vertical velocity ≥ 1 cm s^{-1}) responsible for particle generation. Differences in the vertical distribution of aerosols as they descend are highlighted for the Southern Ocean (purple) and sub-tropics (gray) based on tendencies highlighted in Figure 3 (comparison modeled after Clarke et al. (1998)).

3.1.3 Southern Ocean Summertime Aerosol Composition Estimations

If new particle formation generated through synoptic uplift (Figure 6) is a major source of FT Aitken aerosols, we expect to find signatures of DMS oxidation products in FT particles sampled during SOCRATES. Ambient aerosol measurements from behind the CVI (Section 2.1) support this speculation and provide additional insights into the size and composition of SO aerosol in the summertime: i) Aitken and the few, small accumulation mode (≤ 0.2 μm) particles occurring in high number concentration samples in the FT are composed primarily of H_2SO_4 with possible contributions from more volatile DMS oxidation products like MSA; ii) the majority of these Aitken particles in the FT are smaller than 0.02 μm in diameter; and iii) accumulation-mode particles (~0.1-0.5 μm) sampled from AC, IC, and SC flight levels are primarily sulfur-based with limited sea spray influence (Twohy et al., 2021).

FT Aitken particle composition is assessed using a particle volatility estimate (Section 2.1) based on the temperature evolution of the ratio between heated and unheated CN, CN_{CVI}/CN (Figure 7). Limited sampling occurred where both high aerosol concentrations were present and CVI temperatures were cycled, requiring our analysis to be expanded beyond RPF cases to all instances where CN ≥ 800 mg^{-1}. Our examination is limited to the FT (Z ≥ 1.5 km) because it is dominated by the Aitken particles of interest (see level-leg median cumulative distributions for AC and MT, Figure S6) and the majority of the CVI temperature cycling experiments occurred in this altitude range.

FT Aitken-dominated samples predominantly contain highly volatile particles. CN_{CVI}/CN decreases with increasing CVI temperature (Figure 7) when the ambient particles (-20 to -15°C, 450-500 hPa in the MT; -5 to 0°C, 750-850 hPa AC) are exposed to CVI maximum temperatures (supplemental text S1) between ~25-60°C. The most dramatic particle number decrease occurs for CVI maximum temperatures above ~25-30°C. Aitken volatilization to sizes below the CN detection limit (0.011 μm) under this imposed CVI temperature range is consistent with previous volatility results for small H_2SO_4 particles (Clarke et al., 1987). H_2SO_4 volatility is a function of particle size with small particles volatilizing at much lower temperatures than larger particles under the same conditions (Orsini et al., 1999). Greater than 30% decreases in diameter have been observed for 0.015 μm diameter particles at 25°C (Orsini et al., 1999) while 0.3 μm particles begin losing mass at ~30°C and completely volatize by 125°C (Clarke, 1991). Conversely, neutralized nss-SO_4 (e.g. ammonium sulfate begins volatilizing above 200°C (Clarke et al., 1987)) and sea spray aerosol (e.g. sodium chloride begins volatilizing at ~600°C (Jennings & O'Dowd, 1990; Jennings et al., 1994)) volatilize at even higher temperatures (Schmid et al., 2002) and do not appear to contribute to the composition of the Aitken particles observed in the FT during SOCRATES (Figure 7).

Not all sizes of pure H_2SO_4 particles will shrink below the CN detection limit within the limited CVI temperature range (~25-60°C) maintained in SOCRATES. H_2SO_4 particles with diameters ≥ 0.035 μm required exposures to temperatures over 90°C for ~0.2 seconds before shrinking to smaller than 0.011 μm (Orsini et al., 1999). The longer residence time during SOCRATES (~2 seconds) likely reduces the temperature required for volatizing H_2SO_4 particles below 0.011 μm. Unless particles are < 0.02 μm, however, it would be difficult to shrink pure sulfuric acid particles below the CN size threshold (0.011 μm) at these temperatures (~30°C) (Orsini et al., 1999). Assuming the observed Aitken particles are H_2SO_4, their volatility at ~25-30°C (Figure 7) suggests the majority of particles are ≤ 0.02 μm. H_2SO_4 particles of comparable sizes have exhibited similar behaviors (i.e. partially evaporating below 30°C) to our observations (Orsini et al., 1999; Schmid et al., 2002).

Volatility signatures were also noted in the size-resolved accumulation mode UHSAS measurements during the campaign, providing additional insight into FT particle composition. Very few accumulation mode particles contribute to the Aitken-dominated FT samples analyzed in this section (≤ 50 mg^{-1}, Figure S7b) and most have diameters ≤ 0.2 μm (Figure S6). However, sufficient UHSAS100 samples occurred during CVI temperature cycles to produce a matched volatility analysis for accumulation mode volatility aerosols (Figure S7). $UHSAS100_{CVI}/UHSAS100$ decreases near ~25-30°C, similar to the CN ratio although likely noisier due to the small number of accumulation mode particles sampled. The similarity of the temperature inflection point for these two volatility ratio curves suggests that small accumulation mode aerosols may share their origin with Aitken aerosols in these high aerosol concentration events and that volatile DMS oxidation products are likely the leading contributor to the composition of the few accumulation mode aerosols occurring in the FT (Figure 3a, c).

The magnitude of the particle size change in the small accumulation mode range (shrinking from 0.1-0.2 μm to below 0.1 μm) potentially signals the presence of aerosol species with even higher volatility than H_2SO_4 (Orsini et al., 1999). The most likely candidate for an additional volatile species contributing to particle composition over the SO is the DMS oxidation product MSA, which has a higher vapor pressure than H_2SO_4 (Berresheim et al., 2002; Mauldin et al., 1999). Relatively large MSA particles (0.16-0.26 μm) volatilize at ~50-60°C (O'Dowd et al., 1997). The equilibrium vapor pressure of MSA depends on the availability of bases and RH

so this temperature range may not be applicable across all conditions (Hodshire et al., 2019). However, it is suggestive that small, recently formed MSA particles can evaporate at 30-35°C during the increased SOCRATES CVI residence time. MSA may also contribute to the separation between the AC and MT volatility curves (Figure 7, S4). Higher Aitken mode concentrations (~CN-UHSAS100, colors in Figure 7, S7a) were found in the MT relative to AC for the few samples available, possibly marking less coagulation and growth occurring after particle formation in the MT which would result in smaller, more volatile particles. These MT particles resided at lower ambient temperatures and slightly lower RH (Figure S6a) which, if MSA was present, could drive MSA to partition preferentially to the particulate phase (Berresheim et al., 2002), dominating the volatility response. While low temperatures favor MSA particulate phase partitioning, low RH does not (Hodshire et al., 2019). Understanding the observed accumulation and Aitken volatility responses and the nuances of their implications about particle composition requires more detailed measurements in future campaigns (e.g. gas composition and Aitken size resolved aerosol concentrations, Section 4).

STEM analysis of micro-impactor substrates taken during ambient CVI sampling during SOCRATES (Twohy et al., 2021) gives us further insight into MBL accumulation mode particle composition. For the cases analyzed, mean percentages show sulfur-based particles dominate the SO summertime accumulation mode (~0.1-0.5 μm) number concentration at all altitudes: 93% AC, 68% IC, and 70% SC. The small remaining number fraction is composed of salt-based sea spray, sometimes enriched with sulfur or other trace compositions. If small amounts of organic material occur in these samples, they are not detectable on the carbon STEM substrate. The dominant, sulfur-based composition of these accumulation-mode particles is consistent with most particles growing from Aitken mode aerosols composed of H_2SO_4 or other DMS oxidation products (Section 1). Implications of Aitken particle growth into accumulation mode sizes will be discussed further in Section 3.2.2.

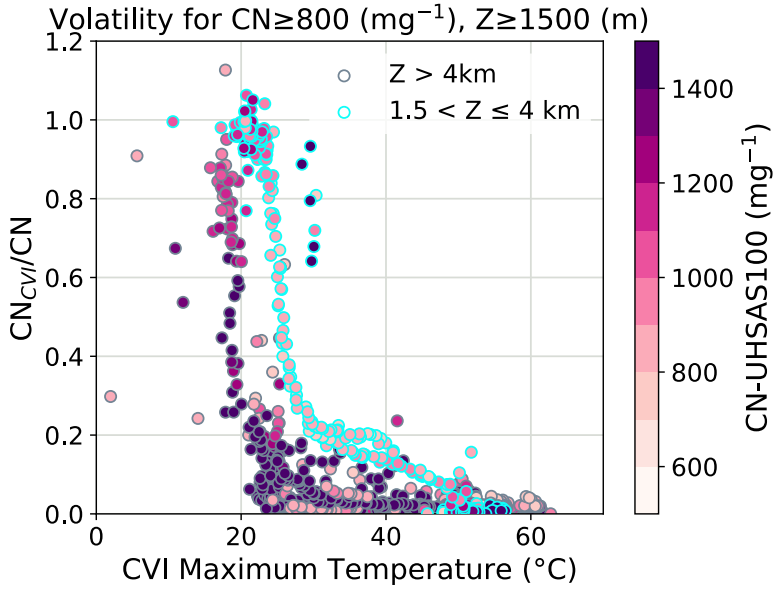

Figure 7 Volatility curves from CVI analysis presented as the ratio between CN and CN_{CVI} versus the maximum temperature of the CVI instrument (supplemental text S1). Points are shown for CN ≥ 800 mg^{-1} above which the small particle concentration is large enough to mark RPF or slightly grown nucleation mode aerosol. Points are limited to FT samples (Z ≥ 1.5 km) due both to limited temperature cycling in the MBL and to targeting Aitken mode dominated environments (Figure S6). Outline colors denote altitude of sample: mid-troposphere (gray) and above cloud (blue). Points are colored by CN-UHSAS100 to estimate the number of particles in the Aitken mode (generally more in the mid-troposphere).

3.2 Controls on Southern Ocean Aerosol and Cloud Droplet Number Concentrations

3.2.1 Average Southern Ocean Aerosol and N_d Structures

To better understand the factors influencing the generation and depletion of aerosols and cloud droplets in the SO and how synoptically generated Aitken particles influence the SO aerosol budget, it is useful to examine the spatial distribution of aerosol and cloud features as sampled by SOCRATES. Flight data is binned by altitude and latitude (Section 2.1) and a multi-flight, campaign average composite is generated for concentrations of aerosol number, aerosol surface area (SA, for coarse and accumulation mode as calculated in Section 2.1), and N_d (Figure 8).

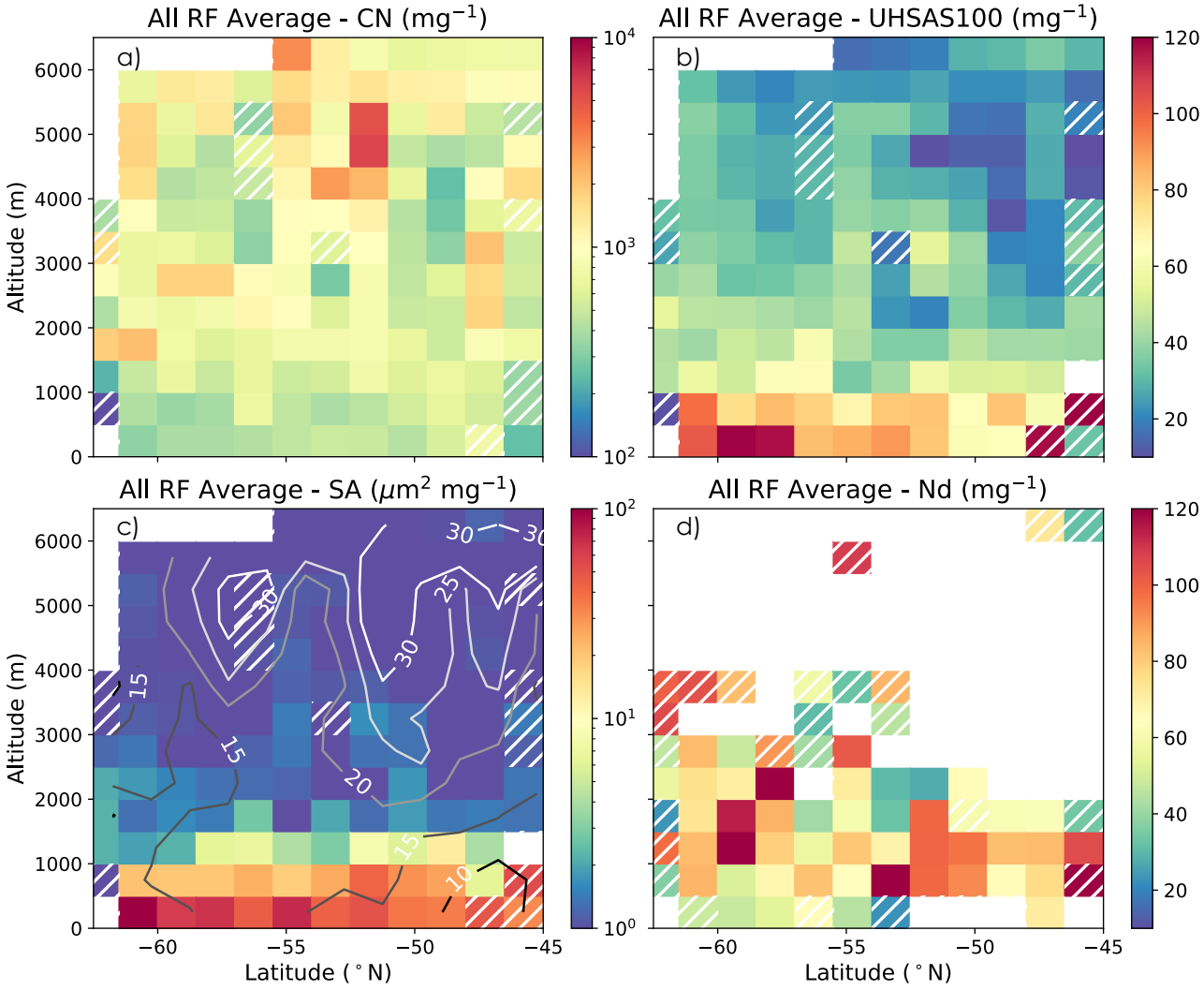

Figure 8 All flight average composites of binned flight medians for 500 m x 1.5° boxes. Aerosol variables are screened for cloud and rain contamination. Number concentrations for (a) total aerosol, (b) accumulation mode aerosol, and (d) cloud droplets are shown along with (c) the surface area concentration computed from accumulation and coarse mode size distributions. Contours of all flight average composite wind speed are also included (c). Bins sampled by 2 or less flights are hatched to indicate inadequate sampling. A companion plot to (d) of cloud droplet number concentration in cm^{-3} units is in Figure S8.

The mean SO CN does not vary significantly with latitude and maintains particle concentrations on the order of ~1000 mg^{-1} in the FT (≥ 1.5 km) and ~500 mg^{-1} in the MBL (< 1.5 km) (Figure 8a). This is consistent with the altitude trend in the CN histograms shown in Figure 3 (d, e, f). The prevalence of consistent high concentrations of CN in the FT across all latitudes suggests synoptic generation (Section 3.1) exerts a widespread influence on SO Aitken mode concentrations.

Accumulation mode number (Figure 8b) and SA (Figure 8c) concentrations both decrease significantly with increasing altitude. SA is largest in the near-surface bins due to increased production of large accumulation and coarse mode aerosols associated with sea spray (see wind speed contours, Figure 8c). Coarse mode particles contribute 2 to 10 times more to total SA in the MBL than accumulation mode (estimated from UHSAS100) while accumulation mode dominates SA in the FT (Figure S9). UHSAS100 concentrations are largest sub-cloud but are less clearly connected to the surface.

SA above ~1.5 km is consistently low enough (SA ≤ 10 $\mu m^2\ mg^{-1}$) to support gas to particle conversion (Clarke et al., 1998; Covert et al., 1996). While low SA is common in the FT, it is rarely observed in the underlying MBL. The single exception occurred during RF13 which sampled an extensive stratocumulus layer under an anticyclonic ridge. In this instance, low SA and high, variable SC CN concentrations were observed in a narrow rift of precipitating shallow cumuli but not in the surrounding stratocumulus-capped MBL. The lack of SC particle formation signatures during SOCRATES is also shown in Figure 3f.

No clear latitudinal dependence in N_d was observed during SOCRATES (Figure 8c) although a slight gradient in CCN was observed (Sanchez et al., 2021). A modest dip at ~55°S in N_d associated with increased precipitation in the mid-latitude storm track is expected in this portion of the SO based on satellite climatology (I. L. McCoy et al., 2020) and is seen in concurrent ship observations of aerosol between 55-60°S (Sanchez et al., 2021). However, the limited amount and spatial distribution of in-cloud sampling during SOCRATES is likely insufficient to capture this nuance of N_d behavior. Cloud observations occur in more altitude bins to the south, either a manifestation of the more frequent occurrence of multi-layered clouds in the southern SO or the more frequent sampling in that region during SOCRATES. Most N_d samples range between 60 and 100 or more mg^{-1} (similar in cm^{-3}, Figure S8) which is consistent with satellite derived N_d climatologically (Bodas-Salcedo et al., 2019; Grosvenor et al., 2018; I. L. McCoy et al., 2020) and instantaneously (Kang et al., 2021) sampled in this region and season.

Qualitatively, we see that the campaign average N_d is comparable to the SC UHSAS100 accumulation-mode aerosol concentration (Figure 8b, d). Quantitatively, N_d and UHSAS100 are correlated at 95% confidence (R=0.6, Figure 9b) when comparing matched time by altitude bins along individual flight composites. Similar distributions occur for matched and total binned flight data for both N_d and UHSAS100, indicating behavior captured in the N_d-UHSAS100 space is representative of SO cloud and aerosol tendencies (Figure 9a, c). Near-cloud UHSAS100 explains 36% of the variance in SO N_d. Consistently higher N_d values for corresponding UHSAS100 (Figure 9a, c) indicates aerosol particles with diameters ≤ 0.1 μm are also activating and contributing to N_d, but poor size-resolved sampling of these particles prevents quantification (see Section 3.2.3 for further discussion). Level-leg median N_d measurements have a stronger relationship with median sub-cloud level leg UHSAS100 (R=0.52) than with above-cloud UHSAS100 (R=0.28) at 95% confidence (Figure S10), indicating SC accumulation mode aerosol significantly influences SO N_d. We next examine the source of this aerosol in the SO.

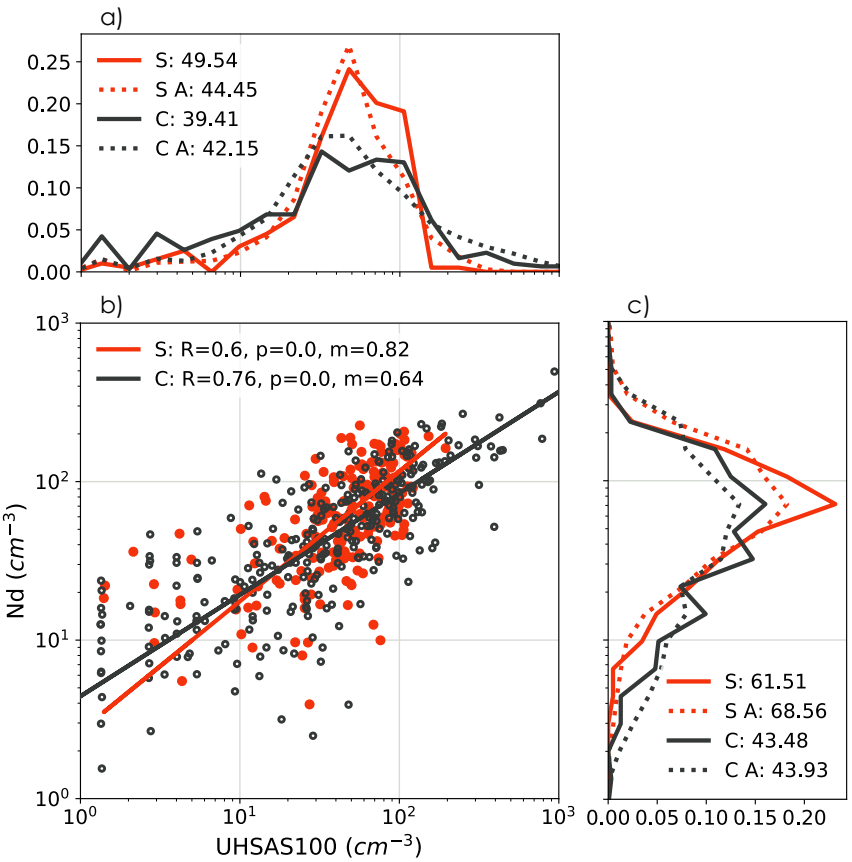

Figure 9 Relationship between accumulation mode and cloud droplet number concentrations in SOCRATES (S, orange) and CSET (C, gray). (b) Altitude (50 m) vs time (2 minutes) bin medians for N_d and UHSAS100 are computed for each flight, matched by space and time, and compared. Pdfs of binned data when both N_d and UHSAS100 are present are shown as solid lines for (a) UHSAS100 and (c) N_d. Pdfs of total, unmatched binned flight data are shown as dashed lines (a, c) and marked with an A. Total data pdfs agree with the behavior of the matched subset. Corresponding median values (a, c), correlation coefficients and p-values (b), and slopes for a log-log fit (b) are included for reference. Few instances of precipitation-depleted N_d or N_d-UHSAS100 points occur (≤ 10 cm^{-3}) in SOCRATES. CSET has a greater number of precipitation-depleted cloud and aerosol features (b, c).

3.2.2 Sources of Accumulation Mode Aerosol in the Southern Ocean

SC accumulation mode aerosol is the principal control on SO N_d (Section 3.2.1). In this pristine region, accumulation mode aerosol particles originate from i) primary sea spray emissions from the surface or ii) growth of Aitken mode aerosols generated through secondary aerosol processes, which can either occur locally in the MBL or in the FT and descend into the SC. Prior work suggests the latter behavior dominates SO summertime CCN (Covert et al., 1996; Korhonen et al., 2008; D. T. McCoy et al., 2015; Quinn et al., 2017; Raes, 1995) and that sea-spray aerosol has only a weak influence on CCN (Modini et al., 2015; Prather et al., 2013; Quinn et al., 2015). SOCRATES provides the opportunity to further test this. Median SC level leg (sampled for ≥ 5 minutes) cumulative distributions (Section 2.1) are calculated and colored by the corresponding median wind speed (Figure 10). Wind speed is a common proxy for estimating sea spray production (Grythe et al., 2014) as well as the magnitude of surface gas fluxes. Correlations are calculated between wind speed and the log of the cumulative number concentration (Grythe et al., 2014) at progressive diameter intervals to understand the influence of wind-speed mechanisms at different aerosol sizes.

Wind-speed dependent production mechanisms are not the main control on small accumulation and Aitken mode concentrations, as exhibited by the lack of correlation when these small particle sizes are included (R for diameters ≥ 0.011, ≥ 0.1 μm in Figure 10). Conversely, coarse (R for ≥ 2.5, ≥ 8.5 μm) and larger accumulation mode (R for ≥ 0.3 μm) aerosol number concentrations are positively and significantly correlated at 95% confidence with wind speed. Thus, larger particles (diameters between 0.3-30 μm) are likely connected to sea spray production mechanisms, consistent with earlier studies (Grythe et al., 2014) (also see Figure 8c).

Enhanced growth associated with increased DMS fluxes (Lana et al., 2011) or increased contributions of submicron organics to sea spray (O'Dowd et al., 2008) may additionally contribute to wind-speed correlations for accumulation and coarse mode aerosols. However, little submicron organic mass was observed in the MBL during concurrent ship sampling and when present it was dominated by sulfate mass (a ratio of 0.2 when submicron organic mass was above its detection limit) (Twohy et al., 2021). This suggests organics have a relatively minor contribution to summertime CCN as measured by SOCRATES, as previously observed for similar SO latitudes (Fossum et al., 2018), although recent work suggests organics have some influence on particles smaller than 0.15 μm (Saliba et al., 2020).

Size ranges that contribute the majority of particles (0.01-0.3 μm), and the majority of the CCN (0.1-0.3 μm), have no relationship with wind speed (Figure 10), consistent with mainly sulfur-based (0.1-0.5 μm diameters) and sulfuric acid (≤ 0.02 μm diameters) composition signatures (Section 3.1.3). FT Aitken aerosols clearly play an essential role in developing SO accumulation mode aerosol and in SO ACI. The nuances of Aitken influence on N_d are discussed in the next section.

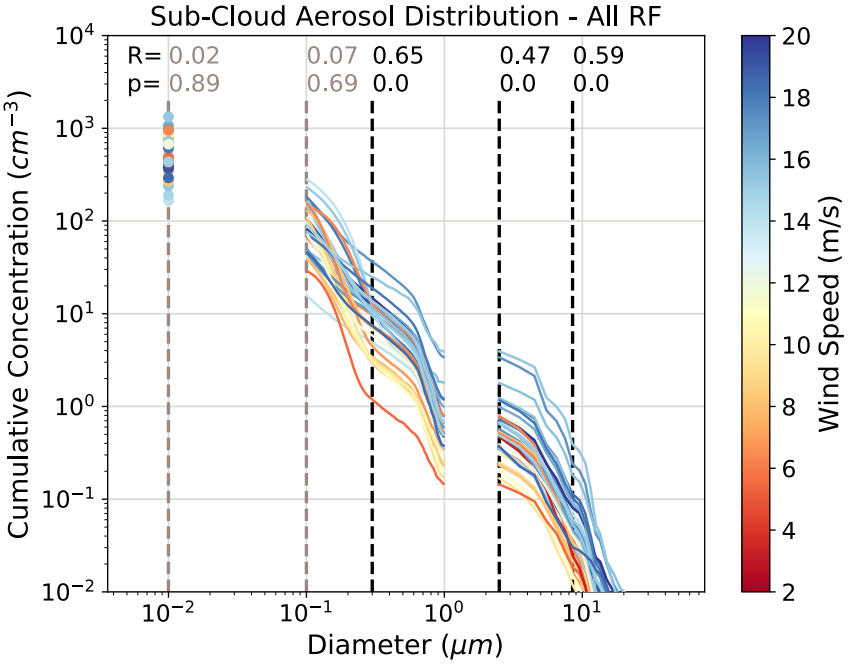

Figure 10 Cumulative size distributions for median sub-cloud level-leg aerosol (calculated for legs with at least 5 minutes of sampling) colored by wind speed at the aircraft (~150 m). Aerosol number concentrations from CN (dots, ≥ 0.01 μm), UHSAS (accumulation, 0.1-1 μm, middle curves), and CDP (coarse, 2.5-30 μm, right curves) are screened for cloud and drizzle. The

cumulative distribution is summed from right to left where CN equals the total number concentration. Correlation coefficients and p-values computed between wind speed and the log of the cumulative number concentrations to the right of the dashed lines are marked (gray for not significant and black for significant at 95% confidence). The relationship between wind speed and log_{10}(cumulative aerosol number concentration) weakens with a decrease in diameter.

3.2.3 Influence of Aitken Mode Aerosols on Southern Ocean Summertime Cloud Droplet Number Concentrations

SOCRATES observations have verified that the FT is a large reservoir of Aitken mode aerosols. Once subsided or entrained into the MBL, these particles may contribute to CCN (Section 3.2.2) and help to modulate SO N_d. Low level clouds in the SO produce a large precipitation sink in N_d and CCN (I. L. McCoy et al., 2020). Despite the magnitude of this sink, relatively high mean SO droplet number concentrations are maintained (N_d ~80-100 cm^{-3}) (I. L. McCoy et al., 2020). For this to be possible, a large and persistent source of CCN must exist over the SO.

The small (≤ 0.02 μm, Section 3.1.3) FT Aitken mode particles brought into the MBL are unlikely to be activated as CCN, even in the stronger updrafts typically occurring in SO marine low clouds. Thus, they likely grow to larger Aitken sizes first, through a combination of condensational growth from the deposition of DMS oxidation products (Ayers et al., 1997; Ayers & Gillett, 2000; Ayers & Gras, 1991; Bates et al., 1998; Charlson et al., 1987) and organic gases (Saliba et al., 2020; Zheng et al., 2020).

A buffering mechanism can occur in response to precipitation sinks. Coalescence scavenging of N_d reduces aerosol number concentration (Wood et al., 2012) and aerosol surface area, leading to increased peak supersaturation during subsequent activation events for a given updraft speed. This results in activation of smaller aerosols, including some of the larger Aitken mode particles which can subsequently grow to accumulation mode sizes through uptake of SO_2 in cloud (Kaufman & Tanré, 1994). Thus, instead of precipitation leading to N_d reduction and eventual cloud breakup (as seen in a low-aerosol, high N_d cloud chamber test by Chandrakar et al. (2017)), the reservoir of FT Aitken aerosol may buffer N_d against precipitation depletion.

Supportive of this hypothesis, we observe fewer precipitation-depleted cloud and aerosol features (N_d, UHSAS100 ≤ 10 cm^{-3}) during SOCRATES relative to CSET (Figure 9). Both campaigns sampled intermittently precipitating shallow cumulus and stratocumulus clouds: SO cyclone cold sectors in SOCRATES and the NEP stratocumulus to trade cumulus transition in CSET. The SO and NEP both experience frequent low cloud precipitation (Leon et al., 2008). Similar near-cloud median accumulation mode aerosol concentrations occurred during SOCRATES (~50 cm^{-3}) and CSET (~40 cm^{-3}) when sampling far from continents (Figure 9a). Despite this, median N_d is higher and less variable during SOCRATES compared to CSET (~70 vs. ~40 cm^{-3}, Figure 9c).

The frequent occurrence of precipitation-depleted clouds (N_d ≤ 10 cm^{-3}) in the cumulus regime west of 140°W defines the lower tail of the N_d CSET pdf (Figure 9c). These 'veil cloud' features are frequently co-located with 'ultra-clean layers' of depleted CCN (UHSAS100 ≤ 10 cm^{-3}) in the subtropics, as seen in Figure 9b. They occur primarily at the detraining tops of cumulus clouds and are developed through collision-coalescence removal of N_d and CCN (O et al., 2018; Wood et al., 2018). The very few instances of N_d ≤ 10 cm^{-3} and/or UHSAS100 ≤ 10 cm^{-3} observed during SOCRATES were associated with: edges of open or cumulus-like cloud (RF02, 06), closed or stratocumulus-like cloud (RF05), or generating cells (RF03, 05); the top, often dissipating cloud layer in a multi-layer cloud (RF02, 06); and samples near snow or mixed phase precipitation (RF03, 06) (Figure S11). Although rarely sampled in SOCRATES,

772 precipitation-depleted mixed-phase cloud and aerosol features may bear future examination.
773 These mixed-phase features are also commonly observed during the winter over the SO (Ahn et
774 al., 2018), when FT Aitken buffering is likely less active due to reduced biological activity in the
775 ocean.
776 N_d and near cloud CCN measured by UHSAS100 are significantly correlated at 95%
777 confidence in both environments, with correlation coefficients $R = 0.6$ in the SO and $R = 0.76$ in
778 the NEP (Figure 9b). As previously noted, the N_d-UHSAS100 relationship captures ACI
779 occurring in these environments, but i) a majority of SO N_d variance is not explained, and ii) SO
780 N_d is often higher than UHSAS100, suggesting Aitken particles are frequently activated.
781 UHSAS100 explains more variance in N_d for CSET than SOCRATES, indicating Aitken
782 particles are less directly important for N_d in the subtropics compared to the SO. These two
783 regions also have significantly different amounts of SC and AC Aitken mode aerosol available: ~
784 200 mg^{-1} median during CSET vs. ~ 500 mg^{-1} during SOCRATES (Figure 3d, f). Supersaturation
785 increases associated with precipitation likely occur in both regions, but the SO has a greater
786 reservoir of MBL Aitken aerosols to prevent major N_d depletion events.
787 These lines of evidence suggest that FT Aitken aerosols act to buffer SO summertime
788 boundary-layer clouds against precipitation depletion of N_d. A possible aerosol life cycle
789 including the hypothesized Aitken-buffering mechanism is depicted in Figure 11 and
790 summarized as follows:
791
792 *I. Marine biogenic outgassing leads to the generation of widespread high*
793 *concentrations of small Aitken-mode aerosols in the FT via lifting, scavenging,*
794 *and cloud outflow nucleation mechanisms (Section 3.1).*
795 *II. Aitken-mode aerosols subside into the SO MBL through horizontal and vertical*
796 *advection and turbulent mixing (Section 1, 3.1.1, 3.2.1).*
797 *III. Once in the MBL, Aitken aerosols grow to accumulation mode sizes through in-*
798 *cloud processing, coagulation, and below-cloud gas condensation (Section 1,*
799 *3.1.3, 3.2.2).*
800 *Aitken-Buffering Mechanism*
801 *IV. SO low clouds precipitate extensively, reducing accumulation-mode aerosol*
802 *through persistent drizzle. This leads to a reduction in boundary-layer CCN and*
803 *an increase in peak cloud-base supersaturation.*
804 *V. The large reservoir of Aitken aerosol in SO MBLs can be activated into CCN,*
805 *buffering N_d against the precipitation-induced depletion commonly seen in*
806 *subtropical MBLs.*
807 *VI. Each activated Aitken aerosol grows by aqueous phase processing into an*
808 *accumulation-mode aerosol, which, upon droplet evaporation, buffers the CCN-*
809 *relevant aerosol number and reduces peak cloud-base supersaturation during*
810 *subsequent activation events.*
811
812 This mechanism is supported by evidence presented in this paper and suggests complex
813 interactions between aerosol and cloud processes that may not be well represented in most
814 current climate models. Aitken-buffering over the mid-latitude oceans has the potential to reduce
815 the frequency of precipitation-depleted cloud features, maintain cloud brightness and longevity,
816 and reduce susceptibility to anthropogenic aerosols in general. More observational analysis and
817 process modeling is required to better quantify Aitken influence on SO N_d characteristics.

Further discussion of the steps needed to test the validity of this mechanism is presented in Section 4.

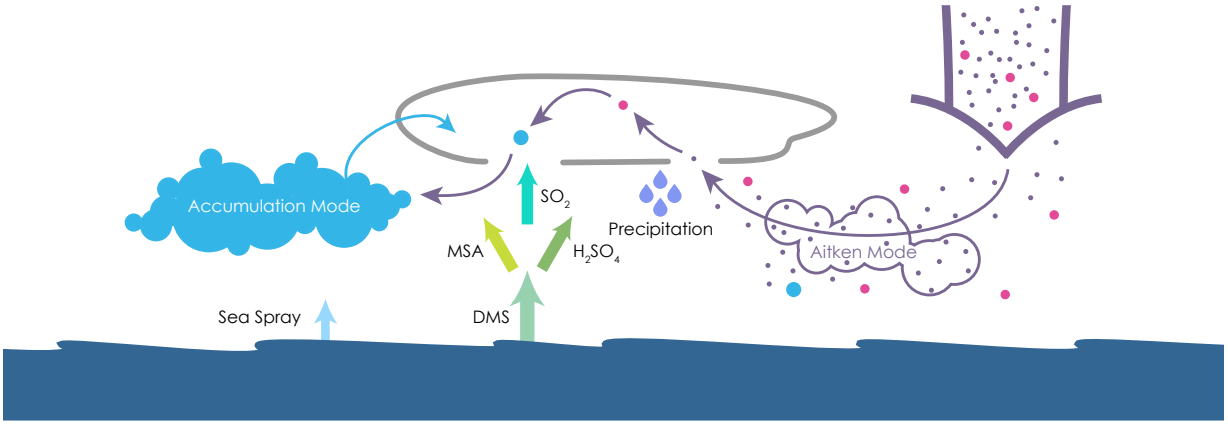

Figure 11 Diagram illustrating hypothetical Aitken-buffering mechanism influencing Southern Ocean clouds. Aitken aerosol (subsided or entrained from the free troposphere) grow in-cloud and sub-cloud to accumulation mode sizes. Precipitation scavenges accumulation-mode aerosol, but this increases peak supersaturation, activating some of the large reservoir of Aitken aerosols to maintain CCN and N_d. This mechanism is an update and extension of aerosol life-cycles identified in the SO (Clarke et al., 1998; Covert et al., 1996; Quinn et al., 2017; Raes, 1995) and has important implications for aerosol-cloud interactions in pristine environments during biologically productive seasons.

3.3 Evaluating Southern Ocean Clouds, Aerosols, and ACI in Global Climate Models

Recent comparisons revealed that many state-of-the-art climate models under-predict N_d over the SO relative to satellite observations (Bodas-Salcedo et al., 2019; I. L. McCoy et al., 2020; Mulcahy et al., 2018; Revell et al., 2019). Identifying inconsistencies between observed and modeled cloud and aerosol characteristics will help to diagnose the underlying cause of this N_d bias. With this purpose, we compare aircraft observations from CSET and SOCRATES with meteorologically nudged CAM6 hindcasts that use prognostic aerosols and cloud droplet concentrations (Section 2.3). Examining CSET simulations allows us to determine a subtropical baseline of model ability and identify model biases unique to the SO. This nudged framework helps us to understand what mechanisms may be contributing to the current N_d bias in models and other discrepancies in ACI while ensuring that differences in the large-scale meteorology are small between the simulation and reality.

CAM6 consistently underpredicts N_d for both campaigns (Figure 12) and has poor correlations with co-located time-height observational composites (R = 0.26 for SOCRATES, none at 95% confidence for CSET, Figure S12). A confounding issue for CSET that does not significantly manifest in SOCRATES is a systematic low bias in CAM6-simulated stratocumulus cloud altitude. Thus, we include an additional comparison pdf for CAM6 in-cloud N_d averaged over all clouds in the MBL along the flight path (CAM6 A in Figure 12a) which adds context to the observationally co-located simulated N_d pdf (CAM6 in Figure 12a). CAM6 N_d for SOCRATES is less than half of observed (CAM6, CAM6 A medians of ~30 vs. ~70 cm^{-3}, a ~55% underestimate) while CSET has a smaller bias (CAM6 ~20, CAM6 A ~30 vs. ~40 cm^{-3} observed, a ~55 or ~25% underestimate).

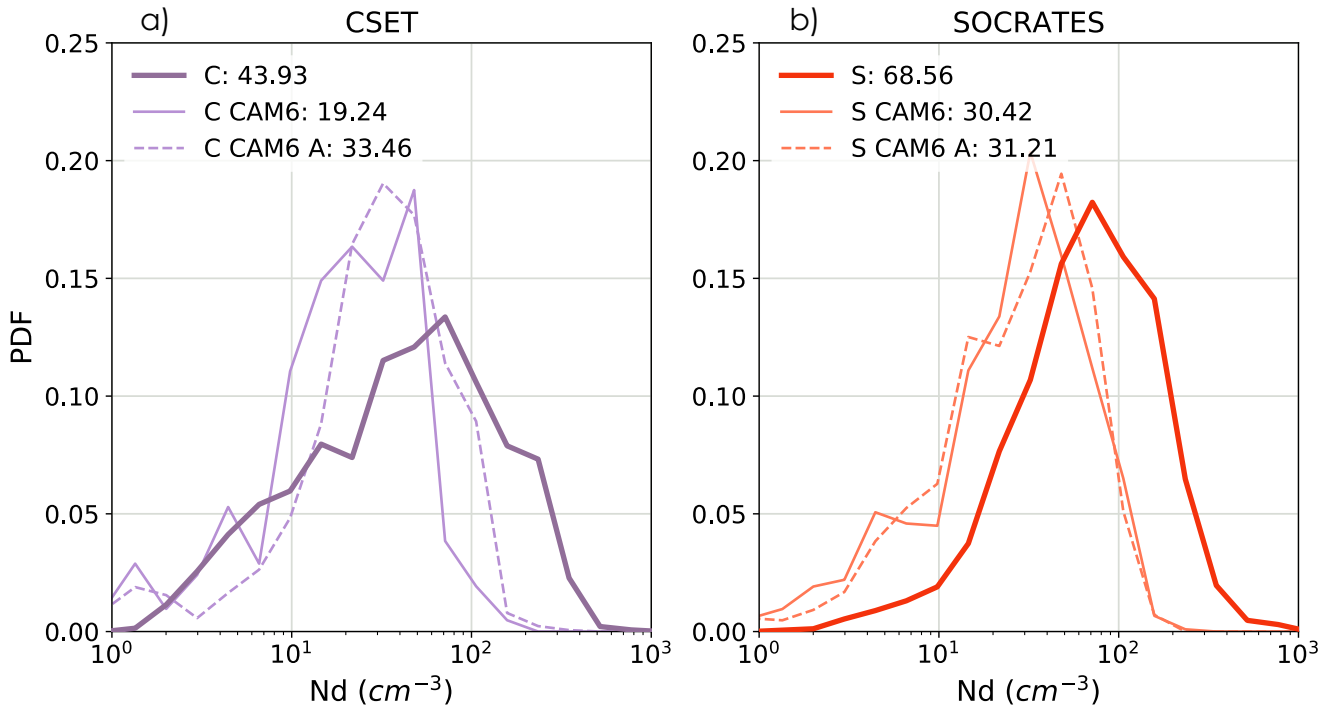

Figure 12 Comparison between observed and simulated N_d values during CSET (a) and SOCRATES (b). Observations and co-located CAM6 output for each flight during CSET and SOCRATES are binned into 50 m by 2 minute bins (Section 2.1). Data are restricted to $Z \leq 4$ km and at a distance from continental effects (S: south of 45°S, C: west of 130°W). Pdfs are shown for all observations during the campaign (solid line, same as dashed line in Figure 9c), CAM6 data that match observations temporally and spatially (CAM6, solid thin line), and all CAM6 data that satisfies the altitude and location criteria (i.e. not matched to observations) (CAM6 A, dashed line). Median values are provided.

Co-located CAM6 aerosol number concentration pdfs sorted by altitude (following Figure 3) show systematic biases in CN and UHSAS100 for both campaigns (Figure 13). CAM6 CSET simulations produce relatively similar SC CN and UHSAS100 pdfs (medians ~15% and ~5% underestimated, Figure 13e, f) but are more biased in the FT: underestimating CN (~45% AC, ~60% MT, Figure 13b, d) and overestimating UHSAS100 (~45% AC, ~80% MT, Figure 13a, c). CAM6 SOCRATES simulations are significantly more biased relative to observations than in the subtropics.

CAM6 SOCRATES CN simulations at all altitudes have a significant low bias compared to observations (~70% SC and MT, ~60% AC, Figure 13b, d, and f). This is despite the MAM4 aerosol scheme in CAM6 including a plausible mechanism for nucleating new aerosol particles from the gas phase (Liu et al., 2016). Insufficient DMS fluxes may be partly responsible for the low CN bias. CAM6 simulated monthly MT CN pdfs for SOCRATES are significantly more biased in February than in January despite similar monthly observational pdfs (underestimate of ~75% vs. ~50%, Figure S13). DMS fluxes sharply decrease between January and February in the

872 climatology used by CAM6 (Lana et al., 2011).

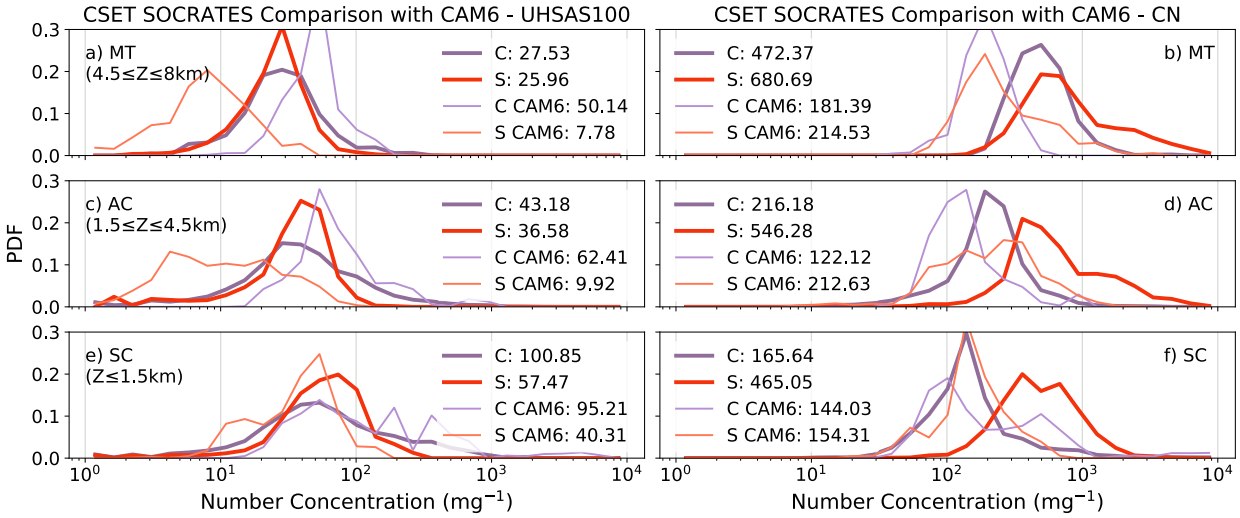

873

874 *Figure 13 As in Figure 3 but including CAM6 aerosol concentrations extracted along the flight tracks (2 min x 50 m binning, as*
875 *in observations).*

876 CAM6 SOCRATES UHSAS100 simulations are also significantly low-biased in the FT
877 (~70%, Figure 13a, c) with a 30% underprediction in the SC (Figure 13e). We expect this bias is
878 inextricably linked to the significant low bias in CAM6 CN in the SO. The CAM6 UHSAS100
879 bias manifests clearly in direct comparisons with time-height binned SOCRATES observations
880 (~50% Figure 14a), impacting the CAM6 low bias in the ratio between UHSAS100-N_d (Figure
881 14b) and likely the low bias in matched N_d (~75%, Figure 14c).

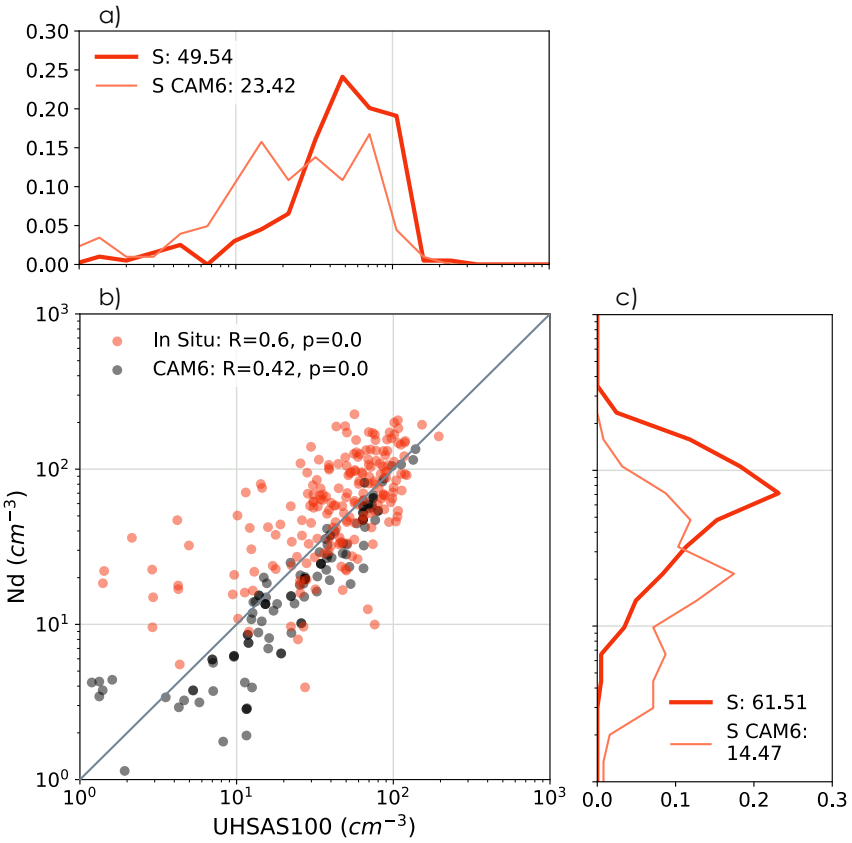

Figure 14 Relationship between SOCRATES accumulation mode and cloud droplet number concentrations as in Figure 9 but including CAM6 collocated to observations (binned into 50 m by 2 minute bins) for each flight (black in b; thin, light orange line in a, c) in addition to observations (orange in b; thick, dark orange line in a, c). Pdfs of number concentrations for matched binned values occurring for CAM6 and observations are shown with median values for UHSAS100 (a) and N_d (c). Scatters of UHSAS100 against N_d (b) are shown along with the correlation coefficients and p-values for in-situ and CAM6 relationships. Data are restricted to $Z \leq 4$ km and in pristine regions south of 45°S.

There are several implications from this model-observation comparison for the issues challenging CAM6's ability to simulate the SO and other pristine environments:

i. Physical mechanisms relevant to generating Aitken aerosols from DMS-oxidation products (which we expect to dominate SO CN) while included in CAM6 (Liu et al., 2016) may be insufficient. CAM6 simulated CN pdfs are both systematically too low at all altitudes in the SO and strikingly similar for CSET and SOCRATES despite the large differences in the observational pdfs and environments for these two campaigns (Figure 13b, d, and f). Even when more DMS is available in the SO (January), high CN concentrations linked to RPF are under-produced (Figure S13). Mechanism discrepancies associated with cloud-outflow particle formation may also lead to the low biased MT CN during CSET (Figure 13b).

ii. Low biases in FT Aitken aerosol (Figure 13b, d) result in insufficient entrainment of particles into the MBL in CAM6 (low biased SC CN, Figure 13f), drastically limiting the ability for FT Aitken aerosol to grow into the main CCN source in the SO summertime (Section 3.2.2, e.g. (Covert et al., 1996; Korhonen et al., 2008; Quinn et al., 2017; Raes, 1995)). This would influence other regions where FT

905 Aitken aerosol is a prominent SC CCN source (e.g. in the northeast Atlantic
906 (Sanchez et al., 2018; Zheng et al., 2018)).
907 iii. Over-production of sea-spray aerosol in CAM6 may compensate on average for
908 low biases in sulfur-based accumulation mode aerosol concentrations connected
909 to low biases in Aitken aerosols in MBL SO summertime. Compared to
910 SOCRATES observations, CAM6 UHSAS100 is 30% lower SC (Figure 13) and
911 50% lower near-cloud (Figure 14a, b) but CAM6 CN is 70% lower SC (Figure
912 13f). This suggests significant surface aerosol contributions to accumulation mode
913 number in CAM6, likely from sea-spray mechanisms, which is inconsistent with
914 observations (Section 3.1.3, 3.2.2) but similar to biases found in other state-of-
915 the-art climate models (Revell et al., 2019).

916
917 CAM6 simulations of SO low clouds are generally fairly skillful (Gettelman et al., 2020;
918 Zhou et al., 2020) but there are some significant cloud-regime specific biases that may also
919 impact simulated SO N_d and should be addressed after the more prescient aerosol biases are
920 resolved. Cloud droplet concentration is affected by an especially complex balance between
921 aerosol sources and sinks (Wood et al., 2012) and the SO is no exception (I. L. McCoy et al.,
922 2020). Precipitation, the major sink, has been overly-active in the SO in past GCMs (Stephens et
923 al., 2010). While precipitation bias is small on average for SOCRATES CAM6 simulations,
924 precipitation is over-produced in cumulus-like clouds and under-produced in stratocumulus
925 clouds (Zhou et al., 2020). CAM6 phase partitioning, particularly production of super-cooled
926 liquid clouds, shows little bias across the campaign (Gettelman et al., 2020; Zhou et al., 2020)
927 but cumulus clouds are excessively glaciated (Atlas et al., 2020). Activation of CCN into N_d is
928 dependent on CCN availability (which we show in this paper has a campaign-wide bias) and
929 turbulent updrafts. CAM6 turbulence agrees with observations in unstable regimes but is under-
930 produced in stable and neutral MBLs (Atlas et al., 2020). Thus, it is likely that in addition to the
931 significant aerosol biases in CAM6, there may be compensating, cloud-regime specific biases
932 between precipitation, glaciation, turbulence and activation that make teasing out the underlying
933 causes of the N_d bias difficult.
934

935 **4 Discussion**

936 SOCRATES observations both confirm and expand upon earlier studies in the SO. The
937 summertime N_d sampled by SOCRATES (median ~ 70 cm^{-3}, Figure 9c) is significantly higher
938 than average MBL N_d sampled in the austral winter slightly to the north of this region (mean ~
939 30 cm^{-3} between 43-45°S) (Ahn et al., 2018). This seasonality is consistent with earlier work
940 linking N_d increases to increased availability of DMS products and aerosol sourced from ocean
941 biology in the SO summertime (Ayers & Gras, 1991; Boers et al., 1998; Charlson et al., 1987; D.
942 T. McCoy et al., 2015; I. L. McCoy et al., 2020).
943 Entrainment and subsidence of FT Aitken particles into the MBL (Covert et al., 1996;
944 Humphries et al., 2016; Sanchez et al., 2021; Schmale et al., 2019) and its central importance as
945 a source for MBL CCN in the SO (Covert et al., 1996; Korhonen et al., 2008; Raes, 1995;
946 Sanchez et al., 2021; Schmale et al., 2019), the NEA (Sanchez et al., 2018; Zheng et al., 2018),
947 and generally between 70°S and 80°N (Quinn et al., 2017) have been previously established.
948 SOCRATES observations of aerosol composition, vertical concentration profiles, and co-located

cloud properties further cements the importance of FT Aitken aerosol influence on SO SC CCN and N_d.

The hypothesized aerosol lifecycle involving the Aitken-buffering mechanism (e.g. synoptic lofting of DMS, particle generation in the FT from DMS-oxidation products, Aitken particle descent into the MBL, Aitken particle growth into accumulation mode sizes below cloud, and increased activation of Aitken particles in response to precipitation depletion) would require large spatial scales. This is consistent with stronger correlations found between DMS fluxes and N_d over large spatial scales (Andreae et al., 1995; Covert et al., 1996; D. T. McCoy et al., 2015) and limited local correlations (Covert et al., 1996).

Future examination of the impact of the Aitken-buffering mechanism on the SO and other pristine environments is needed. The Aitken-buffering mechanism may influence other pristine biologically productive marine regions (e.g. the northeast Atlantic (Sanchez et al., 2018; Zheng et al., 2018)), especially given the importance of entrained FT aerosol on CCN globally (Quinn et al., 2017). The influence of this mechanism should be considered in evaluating the susceptibility of pristine clouds to anthropogenic aerosol (Carslaw et al., 2013) and in constraining radiative forcing associated with ACI (Bellouin et al., 2020; I. L. McCoy et al., 2020; Regayre et al., 2019). The feasibility of entrained FT Aitken particles buffering the CCN budget will be determined by the balance between the rate of precipitation depletion of N_d compared to the rate of Aitken mode activation and growth to cloud affecting sizes. This time scale, as well as general mechanism robustness, could be examined using aerosol-coupled large eddy simulations supported by SO aerosol and cloud observations but would not be easily observable alone. Future examinations should also address the role of mixed-phase and super-cooled cloud physics on SO ACI, impacting the generalizability of the Aitken-buffering mechanism to other pristine environments. How the presence of giant CCN (Jensen & Nugent, 2017) in the SO (McFarquhar et al., 2020) influences supersaturation changes, and subsequent Aitken activation, in response to precipitation removal is also worth examining.

Additional observations contrasting biologically active (summer) and inactive (winter) seasons in the SO can help us to further document ACI in this region. It is critical that future SO aircraft campaigns capture Aitken as well as accumulation mode size distributions and concurrently measure aerosol composition and trace gas species (e.g. DMS, H_2SO_4, and MSA), and how they vary with altitude and boundary-layer regime. Measurements of DMS and precursor gases at the surface and aloft would enable rate calculations and estimates of processing time for aerosol formation, growth, and depletion as well as an estimation of the degree of long-range influence phytoplankton can exert on SO clouds and aerosols.

This paper illustrates some of the complexities of SO aerosol production and growth and underlines the importance of understanding and representing these mechanisms in GCMs. Simulating both mechanisms highlighted in this paper (FT Aitken production through synoptic-uplift and Aitken-buffering in the MBL) requires a good model of relevant marine biogenic emissions. However, neglecting natural new particle formation in GCMs leads to overestimation in the magnitude of the radiative forcing associated with ACI (Gordon et al., 2017). Thus, inclusion of these mechanisms will likely advance the simulation of SO ACI and reduce associated radiative biases, further constraining radiative forcing associated with ACI (Bodas-Salcedo et al., 2019; I. L. McCoy et al., 2020; Regayre et al., 2019).

5 Summary

Observations from the 2018 SOCRATES campaign suggest that new particle formation is widespread and frequent in the summertime Southern Ocean free troposphere (FT, 3-6 km) and dominates the aerosol characteristics of that region. Typical observed signatures of recent particle formation (RPF) events included high and rapidly varying concentrations of total aerosol number concentrations (diameters ≥ 0.011 μm, CN ≥ 1000 mg^{-1}), low accumulation and coarse mode aerosol surface area (diameters 0.1-50 μm, SA ≤ 10 μm^2 mg^{-1}), and low accumulation-mode aerosol number concentrations (diameters 0.1-1 μm, UHSAS100 ≤ 80 mg^{-1}). FT Aitken mode particles (diameters ≤ 0.1 μm) showed volatility signatures of H_2SO_4 or more volatile DMS-oxidation products.

Back-trajectory analysis of RPF classified events (CN ≥ 2500 mg^{-1}) showed air masses had recently ascended from below 1 km to the FT at synoptic rates ($w \geq 1$ cm s^{-1}). Warm-conveyor belts and sub-polar vortices were the two main synoptic drivers of this ascent seen in the SO FT. Broadly, these RPF events are described by a synoptic uplift mechanism for particle generation: boundary-layer air parcels rich in marine biogenic gases (i.e. DMS) are swept up via synoptic motions through cloud, precipitation scavenges large aerosols and reduces aerosol SA, and gas-to-particle conversion occurs in the FT upon cloud exit once DMS oxidizes into precursor gases (e.g. SO_2, H_2SO_4, and MSA). This proposed mechanism explains the prevalence and high concentration of FT Aitken aerosols observed over the SO by SOCRATES, works in concert with other cloud outflow particle formation mechanisms occurring at lower altitudes in the SO (Clarke et al., 1998), and will be active mainly in summer since outgassing of DMS from a biologically active ocean is essential.

Aitken-mode aerosol concentrations are nearly as high in the summertime SO MBL as in the FT and substantially higher than in remote parts of the marine subtropics (i.e. the CSET campaign in the northeast Pacific). Sub-cloud aerosol distributions and correlations with wind speed corroborate earlier work showing sea spray aerosol does not control CCN number over the summertime SO (e.g. Quinn et al. (2017)). Instead, patterns of aerosol number concentrations, size distributions, and compositions (Twohy et al., 2021) support the dominant source of sub-cloud CCN and driver of SO N_d is entrainment and subsequent growth of Aitken aerosol from the large FT reservoir (e.g. (Bates et al., 1998; Covert et al., 1996; Humphries et al., 2016; Korhonen et al., 2008; Quinn et al., 2017; Raes, 1995)).

After entraining into the MBL, the high SO concentrations of Aitken aerosol may buffer N_d and CCN against the effects of precipitation. Precipitation scavenging activates more MBL Aitken aerosol (continuously sourced from the FT and grown within the MBL) to combat this sink of accumulation-mode aerosol and resist depletion of N_d. Lack of precipitation-depleted cloud features during SOCRATES and consistently high N_d in the SO despite a significant precipitation sink (I. L. McCoy et al., 2020) are evidence for this hypothesized Aitken-buffering mechanism. Observations from the subtropical northeast Pacific, where Aitken concentrations just above and within the MBL are much lower than in the SO, show contrasting behavior (e.g. frequent precipitation-depleted cloud features).

Meteorologically nudged CAM6 simulations for SOCRATES show significant low biases in N_d; free tropospheric, near cloud, and (to a lesser extent) sub-cloud accumulation mode aerosol; and Aitken mode aerosol concentrations at all altitudes in the SO. Over-production of sea-spray aerosol at the surface (e.g. Revell et al. (2019)) may mask accumulation mode bias in CAM6 associated with insufficient FT Aitken aerosol production and subsequent entrainment into the SO MBL, where it is essential for growing sulfur-based CCN. Simulated SO and

subtropical aerosol behavior are extremely similar despite large regional differences in the real world. We conclude that while CAM6 includes simplified representations of the aerosol, cloud, and marine biogenic emission processes — whose importance we highlight in this paper — further improvements must be made in CAM6 to achieve quantitative accuracy in simulating the aerosol-cloud interactions and typical, seasonally-varying range of N_d over the summertime SO. SO N_d biases in other state-of-the-art climate models suggest they also need such improvements in simulating pristine environments, which can be informed by detailed SO field studies such as SOCRATES (Bodas-Salcedo et al., 2019; I. L. McCoy et al., 2020; Revell et al., 2019)).

Acknowledgments

The authors wish to thank Mike Reeves for help in interpreting aerosol observations. They further thank Rachel Atlas, Cristina McCluskey, Matt Wyant, Roger Marchand, Xiaoli Zhou, Litai Kang, Kevin Sanchez, and the SOCRATES team for productive discussions of this work.

The National Science Foundation supports the SOCRATES campaign and its continued research efforts (AGS-1660609). Additionally, CHT acknowledges funding through grant AGS-1660605.

ILM, CSB, and RW developed scientific hypothesis, method of approach, and wrote the paper. ILM obtained and analyzed data, ran HYSPLIT trajectories, and extracted model data to match observations. CHT and DWT helped to interpret volatility estimates. AG and CB supplied CAM6 nudged simulations for CSET and SOCRATES. All authors contributed to writing and editing the paper.

Data Availability

NCAR EOL provided aircraft data from the SOCRATES campaign (UCAR/NCAR, 2019) and CSET campaign (UCAR/NCAR, 2017). All information and datasets can be found through the supporting EOL websites (https://www.eol.ucar.edu/field_projects/socrates and http://catalog.eol.ucar.edu/cset). HYSPLIT Back Trajectories were calculated from SOCRATES positions using the publicly available HYSPLIT code (https://www.ready.noaa.gov/HYSPLIT.php). ERA5 Reanalysis products are accessible through the online database at ECMWF (https://www.ecmwf.int/en/forecasts/datasets/reanalysis-datasets/era5). CAM6 simulations for SOCRATES and CSET are available online at https://doi.org/10.5281/zenodo.4480387 (I. L. McCoy et al., 2021).

References

Ahn, E., Huang, Y., Siems, S. T., & Manton, M. J. (2018). A Comparison of Cloud Microphysical Properties Derived From MODIS and CALIPSO With In Situ Measurements Over the Wintertime Southern Ocean. *Journal of Geophysical Research: Atmospheres, 123*(19), 11,120-111,140. <Go to ISI>://WOS:000448374800020

Albrecht, B., Ghate, V., Mohrmann, J., Wood, R., Zuidema, P., Bretherton, C., et al. (2019). Cloud System Evolution in the Trades-CSET: Following the Evolution of Boundary Layer Cloud Systems with the NSF/NCAR GV. *Bull Am Meteorol Soc, 100*(1), 93-121. https://www.ncbi.nlm.nih.gov/pubmed/32042201

1078 Andreae, M. O., Elbert, W., & de Mora, S. J. (1995). Biogenic sulfur emissions and aerosols over the tropical South
1079 Atlantic: 3. Atmospheric dimethylsulfide, aerosols and cloud condensation nuclei. *Journal of Geophysical*
1080 *Research, 100*(D6), 11335-11356. <Go to ISI>://WOS:A1995RF05100024

1081 Andreae, M. O., Jones, C. D., & Cox, P. M. (2005). Strong present-day aerosol cooling implies a hot future. *Nature,*
1082 *435*(7046), 1187-1190. Article. https://www.ncbi.nlm.nih.gov/pubmed/15988515

1083 Atlas, R. L., Bretherton, C. S., Blossey, P. N., Gettelman, A., Bardeen, C., Lin, P., & Ming, Y. (2020). How Well
1084 Do Large-Eddy Simulations and Global Climate Models Represent Observed Boundary Layer Structures
1085 and Low Clouds Over the Summertime Southern Ocean? *Journal of Advances in Modeling Earth Systems,*
1086 *12*(11).

1087 Ayers, G. P., Cainey, J. M., Gillett, R. W., & Ivey, J. P. (1997). Atmospheric sulphur and cloud condensation nuclei
1088 in marine air in the Southern Hemisphere. *Philosophical Transactions of the Royal Society of London*
1089 *Series B-Biological Sciences, 352*(1350), 203-211. <Go to ISI>://WOS:A1997WM31700014

1090 Ayers, G. P., & Gillett, R. W. (2000). DMS and its oxidation products in the remote marine atmosphere:
1091 implications for climate and atmospheric chemistry. *Journal of Sea Research, 43*(3-4), 275-286. <Go to
1092 ISI>://WOS:000089555600011

1093 Ayers, G. P., & Gras, J. L. (1991). Seasonal relationship between cloud condensation nuclei and aerosol
1094 methanesulphonate in marine air. *Nature, 353*(6347), 834-835. <Go to ISI>://WOS:A1991GM73200055
1095 http://www.nature.com/nature/journal/v353/n6347/pdf/353834a0.pdf

1096 Bates, T. S. (2002). Regional marine boundary layer aerosol size distributions in the Indian, Atlantic, and Pacific
1097 Oceans: A comparison of INDOEX measurements with ACE-1, ACE-2, and Aerosols99. *Journal of*
1098 *Geophysical Research, 107*(D19), INX2 25-21-INX22 25-15.
1099 https://agupubs.onlinelibrary.wiley.com/doi/abs/10.1029/2001JD001174

1100 Bates, T. S., Kapustin, V. N., Quinn, P. K., Covert, D. S., Coffman, D. J., Mari, C., et al. (1998). Processes
1101 controlling the distribution of aerosol particles in the lower marine boundary layer during the First Aerosol
1102 Characterization Experiment (ACE 1). *Journal of Geophysical Research: Atmospheres, 103*(D13), 16369-
1103 16383.

1104 Bellouin, N., Quaas, J., Gryspeerdt, E., Kinne, S., Stier, P., Watson-Parris, D., et al. (2020). Bounding Global
1105 Aerosol Radiative Forcing of Climate Change. *Rev Geophys, 58*(1), e2019RG000660.
1106 https://www.ncbi.nlm.nih.gov/pubmed/32734279

1107 Berresheim, H., Elste, T., Tremmel, H. G., Allen, A. G., Hansson, H.-C., Rosman, K., et al. (2002). Gas-aerosol
1108 relationships of H2SO4, MSA, and OH: Observations in the coastal marine boundary layer at Mace Head,
1109 Ireland. *Journal of Geophysical Research, 107*(D19). <Go to ISI>://WOS:000180428300008

1110 Bigg, E. K. (2007). Sources, nature and influence on climate of marine airborne particles. *Environmental Chemistry,*
1111 *4*(3), 155-161. <Go to ISI>://WOS:000247436800004

1112 Bigg, E. K., & Leck, C. (2008). The composition of fragments of bubbles bursting at the ocean surface. *Journal of*
1113 *Geophysical Research, 113*(D11). <Go to ISI>://WOS:000256811300002

1114 Bodas-Salcedo, A., Hill, P. G., Furtado, K., Williams, K. D., Field, P. R., Manners, J. C., et al. (2016). Large
1115 Contribution of Supercooled Liquid Clouds to the Solar Radiation Budget of the Southern Ocean. *Journal*
1116 *of Climate, 29*(11), 4213-4228. <Go to ISI>://WOS:000377116500003

1117 Bodas-Salcedo, A., Mulcahy, J. P., Andrews, T., Williams, K. D., Ringer, M. A., Field, P. R., & Elsaesser, G. S.
1118 (2019). Strong Dependence of Atmospheric Feedbacks on Mixed-Phase Microphysics and Aerosol-Cloud

Interactions in HadGEM3. *J Adv Model Earth Syst, 11*(6), 1735-1758. https://www.ncbi.nlm.nih.gov/pubmed/31598189

Bodas-Salcedo, A., Williams, K. D., Field, P. R., & Lock, A. P. (2012). The Surface Downwelling Solar Radiation Surplus over the Southern Ocean in the Met Office Model: The Role of Midlatitude Cyclone Clouds. *Journal of Climate, 25*(21), 7467-7486. Article. <Go to ISI>://WOS:000311002700009

Bodas-Salcedo, A., Williams, K. D., Ringer, M. A., Beau, I., Cole, J. N. S., Dufresne, J. L., et al. (2014). Origins of the Solar Radiation Biases over the Southern Ocean in CFMIP2 Models*. *Journal of Climate, 27*(1), 41-56. Article. <Go to ISI>://WOS:000329276000003

Boers, R., Jensen, J. B., & Krummel, P. B. (1998). Microphysical and short-wave radiative structure of stratocumulus clouds over the Southern Ocean: Summer results and seasonal differences. *Quarterly Journal of the Royal Meteorological Society, 124*(545), 151-168. <Go to ISI>://WOS:000072056700006

Bretherton, C. S., McCoy, I. L., Mohrmann, J., Wood, R., Ghate, V., Gettelman, A., et al. (2019). Cloud, Aerosol, and Boundary Layer Structure across the Northeast Pacific Stratocumulus?Cumulus Transition as Observed during CSET. *Monthly Weather Review, 147*(6), 2083-2103. https://journals.ametsoc.org/view/journals/mwre/147/6/mwr-d-18-0281.1.xml

Carslaw, K. S., Lee, L. A., Reddington, C. L., Pringle, K. J., Rap, A., Forster, P. M., et al. (2013). Large contribution of natural aerosols to uncertainty in indirect forcing. *Nature, 503*(7474), 67-71. Article. https://www.ncbi.nlm.nih.gov/pubmed/24201280

Catto, J. L., Madonna, E., Joos, H., Rudeva, I., & Simmonds, I. (2015). Global Relationship between Fronts and Warm Conveyor Belts and the Impact on Extreme Precipitation*. *Journal of Climate, 28*(21), 8411-8429. <Go to ISI>://WOS:000363766200007

Chand, D., Wood, R., Ghan, S. J., Wang, M., Ovchinnikov, M., Rasch, P. J., et al. (2012). Aerosol optical depth increase in partly cloudy conditions. *Journal of Geophysical Research: Atmospheres, 117*(D17), n/a-n/a. <Go to ISI>://WOS:000308892800003

Chandrakar, K. K., Cantrell, W., Ciochetto, D., Karki, S., Kinney, G., & Shaw, R. A. (2017). Aerosol removal and cloud collapse accelerated by supersaturation fluctuations in turbulence. *Geophysical Research Letters, 44*(9), 4359-4367. <Go to ISI>://WOS:000402143700047

Charlson, R. J., Lovelock, J. E., Andreae, M. O., & Warren, S. G. (1987). Oceanic phytoplankton, atmospheric sulphur, cloud albedo and climate. *Nature, 326*(6114), 655-661. Review. <Go to ISI>://WOS:A1987G890600046

Clarke, A. D. (1991). A thermo-optic technique for in situ analysis of size-resolved aerosol physicochemistry. *Atmospheric Environment. Part A. General Topics, 25*(3-4), 635-644. http://www.sciencedirect.com/science/article/pii/096016869190061B

Clarke, A. D. (1993). Atmospheric nuclei in the Pacific midtroposphere: Their nature, concentration, and evolution. *Journal of Geophysical Research, 98*(D11), 20633-20647. <Go to ISI>://WOS:A1993MJ29800026

Clarke, A. D., Ahlquist, N. C., & Covert, D. S. (1987). The Pacific marine aerosol: Evidence for natural acid sulfates. *Journal of Geophysical Research: Atmospheres, 92*(D4), 4179-4190. https://agupubs.onlinelibrary.wiley.com/doi/abs/10.1029/JD092iD04p04179

Clarke, A. D., Varner, J. L., Eisele, F., Mauldin, R. L., Tanner, D., & Litchy, M. (1998). Particle production in the remote marine atmosphere: Cloud outflow and subsidence during ACE 1. *Journal of Geophysical Research: Atmospheres, 103*(D13), 16397-16409. <Go to ISI>://WOS:000074828200032

1160 Clement, C. F., Ford, I. J., Twohy, C. H., Weinheimer, A., & Campos, T. (2002). Particle production in the outflow
1161 of a midlatitude storm. *Journal of Geophysical Research: Atmospheres, 107*(D21), AAC 5-1-AAC 5-9.
1162 <Go to ISI>://WOS:000180860300011

1163 Covert, D. S., Kapustin, V. N., Bates, T. S., & Quinn, P. K. (1996). Physical properties of marine boundary layer
1164 aerosol particles of the mid-Pacific in relation to sources and meteorological transport. *Journal of*
1165 *Geophysical Research: Atmospheres, 101*(D3), 6919-6930. <Go to ISI>://WOS:A1996UB98600018

1166 Dunne, E. M., Gordon, H., Kurten, A., Almeida, J., Duplissy, J., Williamson, C., et al. (2016). Global atmospheric
1167 particle formation from CERN CLOUD measurements. *Science, 354*(6316), 1119-1124.
1168 https://www.ncbi.nlm.nih.gov/pubmed/27789796

1169 Eckhardt, S., Stohl, A., Wernli, H., James, P., Forster, C., & Spichtinger, N. (2004). A 15-Year Climatology of
1170 Warm Conveyor Belts. *Journal of Climate, 17*(1), 218-237. <Go to ISI>://WOS:000187742400016

1171 Fitzgerald, J. W. (1991). Marine aerosols: A review. *Atmospheric Environment. Part A. General Topics, 25*(3-4),
1172 533-545. <Go to ISI>://WOS:A1991FF35800002

1173 Forster, P. M. (2016). Inference of Climate Sensitivity from Analysis of Earth's Energy Budget. *Annual Review of*
1174 *Earth and Planetary Sciences, 44*(1), 85-106. <Go to ISI>://WOS:000379329700005

1175 Fossum, K. N., Ovadnevaite, J., Ceburnis, D., Dall'Osto, M., Marullo, S., Bellacicco, M., et al. (2018). Summertime
1176 Primary and Secondary Contributions to Southern Ocean Cloud Condensation Nuclei. *Scientific Reports,*
1177 *8*(1), 13844. https://www.ncbi.nlm.nih.gov/pubmed/30218089

1178 Gelaro, R., McCarty, W., Suarez, M. J., Todling, R., Molod, A., Takacs, L., et al. (2017). The Modern-Era
1179 Retrospective Analysis for Research and Applications, Version 2 (MERRA-2). *J Clim, Volume 30*(Iss 13),
1180 5419-5454. https://www.ncbi.nlm.nih.gov/pubmed/32020988

1181 Gettelman, A., Bardeen, C. G., McCluskey, C. S., Järvinen, E., Stith, J., Bretherton, C., et al. (2020). Simulating
1182 Observations of Southern Ocean Clouds and Implications for Climate. *Journal of Geophysical Research:*
1183 *Atmospheres, 125*(21). <Go to ISI>://WOS:000591896900002
1184 https://agupubs.onlinelibrary.wiley.com/doi/10.1029/2020JD032619

1185 Gordon, H., Kirkby, J., Baltensperger, U., Bianchi, F., Breitenlechner, M., Curtius, J., et al. (2017). Causes and
1186 importance of new particle formation in the present-day and preindustrial atmospheres. *Journal of*
1187 *Geophysical Research: Atmospheres, 122*(16), 8739-8760. <Go to ISI>://WOS:000416382800021

1188 Grosvenor, D. P., Sourdeval, O., Zuidema, P., Ackerman, A., Alexandrov, M. D., Bennartz, R., et al. (2018).
1189 Remote Sensing of Droplet Number Concentration in Warm Clouds: A Review of the Current State of
1190 Knowledge and Perspectives. *Rev Geophys, 56*(2), 409-453.
1191 https://www.ncbi.nlm.nih.gov/pubmed/30148283

1192 Grythe, H., Ström, J., Krejci, R., Quinn, P., & Stohl, A. (2014). A review of sea-spray aerosol source functions using
1193 a large global set of sea salt aerosol concentration measurements. *Atmospheric Chemistry and Physics,*
1194 *14*(3), 1277-1297. <Go to ISI>://WOS:000332384900009

1195 Hamilton, D. S., Lee, L. A., Pringle, K. J., Reddington, C. L., Spracklen, D. V., & Carslaw, K. S. (2014).
1196 Occurrence of pristine aerosol environments on a polluted planet. *Proc Natl Acad Sci U S A, 111*(52),
1197 18466-18471. Article. https://www.ncbi.nlm.nih.gov/pubmed/25512511

1198 Hobbs, P. V. (1971). Simultaneous airborne measurements of cloud condensation nuclei and sodium-containing
1199 particles over the ocean. *Quarterly Journal of the Royal Meteorological Society, 097*(413), 263-271. <Go
1200 to ISI>://WOS:A1971K009800001

1201 Hodshire, A. L., Campuzano-Jost, P., Kodros, J. K., Croft, B., Nault, B. A., Schroder, J. C., et al. (2019). The
1202 potential role of methanesulfonic acid (MSA) in aerosol formation and growth and the associated radiative
1203 forcings. *Atmospheric Chemistry and Physics, 19*(5), 3137-3160. <Go to ISI>://WOS:000460947700002

1204 Holton, J. R., & Haikm, G. J. (2013). *An Introduction to Dynamic Meteorology* (Fifth ed.). Academic Press:
1205 Elseveir.

1206 Humphries, R. S., Klekociuk, A. R., Schofield, R., Keywood, M., Ward, J., & Wilson, S. R. (2016). Unexpectedly
1207 high ultrafine aerosol concentrations above East Antarctic sea ice. *Atmospheric Chemistry and Physics,*
1208 *16*(4), 2185-2206. <Go to ISI>://WOS:000372971500021

1209 Jennings, S. G., & O'Dowd, C. D. (1990). Volatility of aerosol at Mace Head, on the west coast of Ireland. *Journal*
1210 *of Geophysical Research: Atmospheres, 95*(D9), 13937-13948.
1211 https://agupubs.onlinelibrary.wiley.com/doi/abs/10.1029/JD095iD09p13937

1212 Jennings, S. G., O'Dowd, C. D., Cooke, W. F., Sheridan, P. J., & Cachier, H. (1994). Volatility of elemental carbon.
1213 *Geophysical Research Letters, 21*(16), 1719-1722.
1214 https://agupubs.onlinelibrary.wiley.com/doi/abs/10.1029/94GL01423

1215 Jensen, J. B., & Nugent, A. D. (2017). Condensational Growth of Drops Formed on Giant Sea-Salt Aerosol
1216 Particles. *Journal of the Atmospheric Sciences, 74*(3), 679-697.

1217 Kang, L., Marchand, R. T., & Smith, W. L. (2021). Evaluation of MODIS and Himawari-8 Low Clouds Retrievals
1218 over the Southern Ocean with In Situ Measurements from the SOCRATES Campaign. *Earth and Space*
1219 *Science, n/a*(n/a), e2020EA001397.
1220 https://agupubs.onlinelibrary.wiley.com/doi/abs/10.1029/2020EA001397

1221 Kaufman, Y. J., & Tanré, D. (1994). Effect of variations in super-saturation on the formation of cloud condensation
1222 nuclei. *Nature, 369*(6475), 45-48. https://doi.org/10.1038/369045a0

1223 Kazil, J., Wang, H., Feingold, G., Clarke, A. D., Snider, J. R., & Bandy, A. R. (2011). Modeling chemical and
1224 aerosol processes in the transition from closed to open cells during VOCALS-REx. *Atmospheric Chemistry*
1225 *and Physics, 11*(15), 7491-7514. Article. <Go to ISI>://WOS:000293826500006

1226 Kerminen, V.-M., Chen, X., Vakkari, V., Petäjä, T., Kulmala, M., & Bianchi, F. (2018). Atmospheric new particle
1227 formation and growth: review of field observations. *Environmental Research Letters, 13*(10). <Go to
1228 ISI>://WOS:000445933100002

1229 Kirkby, J., Curtius, J., Almeida, J., Dunne, E., Duplissy, J., Ehrhart, S., et al. (2011). Role of sulphuric acid,
1230 ammonia and galactic cosmic rays in atmospheric aerosol nucleation. *Nature, 476*(7361), 429-433.
1231 https://www.ncbi.nlm.nih.gov/pubmed/21866156

1232 Korhonen, H., Carslaw, K. S., Spracklen, D. V., Mann, G. W., & Woodhouse, M. T. (2008). Influence of oceanic
1233 dimethyl sulfide emissions on cloud condensation nuclei concentrations and seasonality over the remote
1234 Southern Hemisphere oceans: A global model study. *Journal of Geophysical Research, 113*(D15). <Go to
1235 ISI>://WOS:000258339000004

1236 Kupc, A., Williamson, C., Wagner, N. L., Richardson, M., & Brock, C. A. (2018). Modification, calibration, and
1237 performance of the Ultra-High Sensitivity Aerosol Spectrometer for particle size distribution and volatility
1238 measurements during the Atmospheric Tomography Mission (ATom) airborne campaign. *Atmospheric*
1239 *Measurement Techniques, 11*(1), 369-383. <Go to ISI>://WOS:000422881100002

1240 Kürten, A., Bianchi, F., Almeida, J., Kupiainen-Määttä, O., Dunne, E. M., Duplissy, J., et al. (2016). Experimental
1241 particle formation rates spanning tropospheric sulfuric acid and ammonia abundances, ion production rates,
1242 and temperatures. *Journal of Geophysical Research: Atmospheres, 121*(20).

1243 Lana, A., Bell, T. G., Simó, R., Vallina, S. M., Ballabrera-Poy, J., Kettle, A. J., et al. (2011). An updated
1244 climatology of surface dimethlysulfide concentrations and emission fluxes in the global ocean. *Global*
1245 *Biogeochemical Cycles, 25*(1), n/a-n/a. <Go to ISI>://WOS:000286755000001

1246 Leon, D. C., Wang, Z., & Liu, D. (2008). Climatology of drizzle in marine boundary layer clouds based on 1 year of
1247 data from CloudSat and Cloud-Aerosol Lidar and Infrared Pathfinder Satellite Observations (CALIPSO).
1248 *Journal of Geophysical Research, 113*.

1249 Liu, X., Ma, P. L., Wang, H., Tilmes, S., Singh, B., Easter, R. C., et al. (2016). Description and evaluation of a new
1250 four-mode version of the Modal Aerosol Module (MAM4) within version 5.3 of the Community
1251 Atmosphere Model. *Geoscientific Model Development, 9*(2), 505-522. <Go to
1252 ISI>://WOS:000376933700003

1253 Mauldin, R. L., Tanner, D. J., Heath, J. A., Huebert, B. J., & Eisele, F. L. (1999). Observations of H2SO4and MSA
1254 during PEM-Tropics-A. *Journal of Geophysical Research: Atmospheres, 104*(D5), 5801-5816.

1255 McCoy, D. T., Burrows, S. M., Wood, R., Grosvenor, D. P., Elliott, S. M., Ma, P. L., et al. (2015). Natural aerosols
1256 explain seasonal and spatial patterns of Southern Ocean cloud albedo. *Sci Adv, 1*(6), e1500157.
1257 https://www.ncbi.nlm.nih.gov/pubmed/26601216

1258 McCoy, I. L., Bretherton, C. S., Wood, R., Twohy, C. H., Gettelman, A., Bardeen, C. G., & Toohey, D. W. (2021).
1259 Supporting data for the manuscript: "Influences of Recent Particle Formation on Southern Ocean Aerosol
1260 Variability and Low Cloud Properties" (Publication no. doi:10.5281/zenodo.4480387).

1261 McCoy, I. L., McCoy, D. T., Wood, R., Regayre, L., Watson-Parris, D., Grosvenor, D. P., et al. (2020). The
1262 hemispheric contrast in cloud microphysical properties constrains aerosol forcing. *Proc Natl Acad Sci U S*
1263 *A, 117*(32), 18998-19006. https://www.ncbi.nlm.nih.gov/pubmed/32719114

1264 McFarquhar, G. M., Bretherton, C., Marchand, R., Protat, A., DeMott, P. J., Alexander, S. P., et al. (2020).
1265 Observations of clouds, aerosols, precipitation, and surface radiation over the Southern Ocean: An
1266 overview of CAPRICORN, MARCUS, MICRE and SOCRATES. *Bulletin of the American Meteorological*
1267 *Society*, 1-92. https://journals.ametsoc.org/view/journals/bams/aop/BAMS-D-20-0132.1/BAMS-D-20-
1268 0132.1.xml

1269 Modini, R. L., Frossard, A. A., Ahlm, L., Russell, L. M., Corrigan, C. E., Roberts, G. C., et al. (2015). Primary
1270 marine aerosol-cloud interactions off the coast of California. *Journal of Geophysical Research:*
1271 *Atmospheres, 120*(9), 4282-4303.

1272 Mulcahy, J. P., Jones, C., Sellar, A., Johnson, B., Boutle, I. A., Jones, A., et al. (2018). Improved Aerosol Processes
1273 and Effective Radiative Forcing in HadGEM3 and UKESM1. *Journal of Advances in Modeling Earth*
1274 *Systems, 10*(11), 2786-2805. <Go to ISI>://WOS:000452864500007

1275 Noone, K. J., Ogren, J. A., Heintzenberg, J., Charlson, R. J., & Covert, D. S. (1988). Design and Calibration of a
1276 Counterflow Virtual Impactor for Sampling of Atmospheric Fog and Cloud Droplets. *Aerosol Science and*
1277 *Technology, 8*(3), 235-244. <Go to ISI>://WOS:A1988N998900004

1278 O, K.-T., Wood, R., & Bretherton, C. S. (2018). Ultraclean Layers and Optically Thin Clouds in the Stratocumulus-
1279 to-Cumulus Transition. Part II: Depletion of Cloud Droplets and Cloud Condensation Nuclei through
1280 Collision–Coalescence. *Journal of the Atmospheric Sciences, 75*(5), 1653-1673. <Go to
1281 ISI>://WOS:000434270600017

1282 O'Dowd, C. D., Langmann, B., Varghese, S., Scannell, C., Ceburnis, D., & Facchini, M. C. (2008). A combined
1283 organic-inorganic sea-spray source function. *Geophysical Research Letters, 35*(1). <Go to
1284 ISI>://WOS:000252182900001

1285 O'Dowd, C. D., Smith, M. H., Consterdine, I. E., & Lowe, J. A. (1997). Marine aerosol, sea-salt, and the marine
1286 sulphur cycle: A short review. *Atmospheric Environment, 31*(1), 73-80. Article. <Go to
1287 ISI>://WOS:A1997VP27300007

1288 Orsini, D. A., Wiedensohler, A., Stratmann, F., & Covert, D. S. (1999). A New Volatility Tandem Differential
1289 Mobility Analyzer to Measure the Volatile Sulfuric Acid Aerosol Fraction. *Journal of Atmospheric and*
1290 *Oceanic Technology, 16*(6), 760-772. <Go to ISI>://WOS:000080802600011

1291 Prather, K. A., Bertram, T. H., Grassian, V. H., Deane, G. B., Stokes, M. D., Demott, P. J., et al. (2013). Bringing
1292 the ocean into the laboratory to probe the chemical complexity of sea spray aerosol. *Proc Natl Acad Sci U S*
1293 *A, 110*(19), 7550-7555. https://www.ncbi.nlm.nih.gov/pubmed/23620519

1294 Quinn, P. K., & Bates, T. S. (2011). The case against climate regulation via oceanic phytoplankton sulphur
1295 emissions. *Nature, 480*(7375), 51-56. https://www.ncbi.nlm.nih.gov/pubmed/22129724

1296 Quinn, P. K., Coffman, D. J., Johnson, J. E., Upchurch, L. M., & Bates, T. S. (2017). Small fraction of marine cloud
1297 condensation nuclei made up of sea spray aerosol. *Nature Geoscience, 10*(9), 674-679. <Go to
1298 ISI>://WOS:000409229600015

1299 Quinn, P. K., Collins, D. B., Grassian, V. H., Prather, K. A., & Bates, T. S. (2015). Chemistry and related properties
1300 of freshly emitted sea spray aerosol. *Chem Rev, 115*(10), 4383-4399.
1301 https://www.ncbi.nlm.nih.gov/pubmed/25844487

1302 Raes, F. (1995). Entrainment of free tropospheric aerosols as a regulating mechanism for cloud condensation nuclei
1303 in the remote marine boundary layer. *Journal of Geophysical Research, 100*(D2), 2893-2903. <Go to
1304 ISI>://WOS:A1995QJ63000013
1305 http://onlinelibrary.wiley.com/store/10.1029/94JD02832/asset/jgrd3417.pdf?v=1&t=il9ui59c&s=0fb373f7ac4989db
1306 34b73c4947cc688497f2fda4

1307 Regayre, L. A., Schmale, J., Johnson, J. S., Tatzelt, C., Baccarini, A., Henning, S., et al. (2019). The value of remote
1308 marine aerosol measurements for constraining radiative forcing uncertainty. *Atmos. Chem. Phys. Discuss.,*
1309 *2019*, 1-11. https://www.atmos-chem-phys-discuss.net/acp-2019-1085/

1310 Revell, L. E., Kremser, S., Hartery, S., Harvey, M., Mulcahy, J. P., Williams, J., et al. (2019). The sensitivity of
1311 Southern Ocean aerosols and cloud microphysics to sea spray and sulfate aerosol production in the
1312 HadGEM3-GA7.1 chemistry–climate model. *Atmospheric Chemistry and Physics, 19*(24), 15447-15466.
1313 <Go to ISI>://WOS:000503444400006

1314 Saliba, G., Sanchez, K. J., Russell, L. M., Twohy, C. H., Roberts, G. C., Lewis, S., et al. (2020). Organic
1315 composition of three different size ranges of aerosol particles over the Southern Ocean. *Aerosol Science*
1316 *and Technology, 55*(3), 268-288. https://doi.org/10.1080/02786826.2020.1845296

1317 Sanchez, K. J., Chen, C. L., Russell, L. M., Betha, R., Liu, J., Price, D. J., et al. (2018). Substantial Seasonal
1318 Contribution of Observed Biogenic Sulfate Particles to Cloud Condensation Nuclei. *Scientific Reports,*
1319 *8*(1), 3235. https://www.ncbi.nlm.nih.gov/pubmed/29459666

1320 Sanchez, K. J., & Roberts, G. (2018). *SOCRATES CCN measurements*.

1321 Sanchez, K. J., Roberts, G. C., Saliba, G., Russell, L. M., Twohy, C., Reeves, M. J., et al. (2021). Measurement
1322 report: Cloud processes and the transport of biological emissions affect southern ocean particle and cloud
1323 condensation nuclei concentrations. *Atmospheric Chemistry and Physics, 21*(5), 3427-3446.

1324 Schmale, J., Baccarini, A., Thurnherr, I., Henning, S., Efraim, A., Regayre, L., et al. (2019). Overview of the
1325 Antarctic Circumnavigation Expedition: Study of Preindustrial-like Aerosols and Their Climate Effects

(ACE-SPACE). *Bulletin of the American Meteorological Society, 100*(11), 2260-2283. https://journals.ametsoc.org/doi/abs/10.1175/BAMS-D-18-0187.1

Schmid, O., Eimer, B., Hagen, D. E., & Whitefield, P. D. (2002). Investigation of Volatility Method for Measuring Aqueous Sulfuric Acid on Mixed Aerosols. *Aerosol Science and Technology, 36*(8), 877-889. <Go to ISI>://WOS:000176493400003

Seinfeld, J. H., & Pandis, S. N. (2016). *Atmospheric Chemistry and Physics : From Air Pollution to Climate Change*. New York, UNITED STATES: John Wiley & Sons, Incorporated.

Stein, A. F., Draxler, R. R., Rolph, G. D., Stunder, B. J. B., Cohen, M. D., & Ngan, F. (2015). NOAA's HYSPLIT Atmospheric Transport and Dispersion Modeling System. *Bulletin of the American Meteorological Society, 96*(12), 2059-2077. <Go to ISI>://WOS:000368500900001

Stephens, G. L., L'Ecuyer, T., Forbes, R., Gettelmen, A., Golaz, J.-C., Bodas-Salcedo, A., et al. (2010). Dreary state of precipitation in global models. *Journal of Geophysical Research: Atmospheres, 115*(D24). <Go to ISI>://WOS:000285642000008

Twohy, C. H., Anderson, J. R., Toohey, D. W., Andrejczuk, M., Adams, A., Lytle, M., et al. (2013). Impacts of aerosol particles on the microphysical and radiative properties of stratocumulus clouds over the southeast Pacific Ocean. *Atmospheric Chemistry and Physics, 13*(5), 2541-2562. <Go to ISI>://WOS:000316960500016

Twohy, C. H., Clement, C. F., Gandrud, B. W., Weinheimer, A. J., Campos, T. L., Baumgardner, D., et al. (2002). Deep convection as a source of new particles in the midlatitude upper troposphere. *Journal of Geophysical Research: Atmospheres, 107*(D21), AAC 6-1-AAC 6-10. <Go to ISI>://WOS:000180860300012

Twohy, C. H., DeMott, P. J., Russell, L. M., Toohey, D. W., Rainwater, B., Geiss, R., et al. (2021). Cloud-Nucleating Particles over the Southern Ocean in a Changing Climate. *Earth's Future, n/a*(n/a), e2020EF001673. https://agupubs.onlinelibrary.wiley.com/doi/abs/10.1029/2020EF001673

Twohy, C. H., Schanot, A. J., & Cooper, W. A. (1997). Measurement of Condensed Water Content in Liquid and Ice Clouds Using an Airborne Counterflow Virtual Impactor. *Journal of Atmospheric and Oceanic Technology, 14*(1), 197-202. <Go to ISI>://WOS:A1997WD27300015

Twomey, S. (1977). The Influence of Pollution on the Shortwave Albedo of Clouds. *Journal of the Atmospheric Sciences, 34*(7), 1149-1152. Note. <Go to ISI>://WOS:A1977DP78800020
http://journals.ametsoc.org/doi/pdf/10.1175/1520-0469%281977%29034%3C1149%3ATIOPOT%3E2.0.CO%3B2

UCAR/NCAR, E. O. L. (2017). *Low Rate (LRT - 1 sps) Navigation, State Parameter, and Microphysics Flight-Level Data (Version 1.2)*.

UCAR/NCAR, E. O. L. (2019). *Low Rate (LRT - 1 sps) Navigation, State Parameter, and Microphysics Flight-Level Data (Version 1.3)*.

Weber, R. J., Chen, G., Davis, D. D., Mauldin, R. L., Tanner, D. J., Eisele, F. L., et al. (2001). Measurements of enhanced H2SO4and 3-4 nm particles near a frontal cloud during the First Aerosol Characterization Experiment (ACE 1). *Journal of Geophysical Research: Atmospheres, 106*(D20), 24107-24117. <Go to ISI>://WOS:000171974000015

Williams, K. D., Bodas-Salcedo, A., Déqué, M., Fermepin, S., Medeiros, B., Watanabe, M., et al. (2013). The Transpose-AMIP II Experiment and Its Application to the Understanding of Southern Ocean Cloud Biases in Climate Models. *Journal of Climate, 26*(10), 3258-3274. <Go to ISI>://WOS:000318775900016

1366 Williamson, C. J., Kupc, A., Axisa, D., Bilsback, K. R., Bui, T., Campuzano-Jost, P., et al. (2019). A large source of
1367 cloud condensation nuclei from new particle formation in the tropics. *Nature, 574*(7778), 399-403.
1368 https://www.ncbi.nlm.nih.gov/pubmed/31619794

1369 Wood, R., Leon, D., Lebsock, M., Snider, J., & Clarke, A. D. (2012). Precipitation driving of droplet concentration
1370 variability in marine low clouds. *Journal of Geophysical Research: Atmospheres, 117*(D19), n/a-n/a.

1371 Wood, R., O, K.-T., Bretherton, C. S., Mohrmann, J., Albrecht, B. A., Zuidema, P., et al. (2018). Ultraclean Layers
1372 and Optically Thin Clouds in the Stratocumulus-to-Cumulus Transition. Part I: Observations. *Journal of the*
1373 *Atmospheric Sciences, 75*(5), 1631-1652. <Go to ISI>://WOS:000434270600016

1374 Zender, C. (2001). Particle Size Distributions: Theory and Application to Aerosols, Clouds, and Soils.

1375 Zheng, G., Kuang, C., Uin, J., Watson, T., & Wang, J. (2020). Large contribution of organics to condensational
1376 growth and formation of cloud condensation nuclei (CCN) in the remote marine boundary layer.
1377 *Atmospheric Chemistry and Physics, 20*(21), 12515-12525.

1378 Zheng, G., Wang, Y., Aiken, A. C., Gallo, F., Jensen, M. P., Kollias, P., et al. (2018). Marine boundary layer aerosol
1379 in the eastern North Atlantic: seasonal variations and key controlling processes. *Atmospheric Chemistry*
1380 *and Physics, 18*(23), 17615-17635. <Go to ISI>://WOS:000452860300004

1381 Zhou, X., Atlas, R., McCoy, I. L., Bretherton, C. S., Bardeen, C., Gettelman, A., et al. (2020). Evaluation of cloud
1382 and precipitation simulations in CAM6 and AM4 using observations over the Southern Ocean. *Earth and*
1383 *Space Science*.
1384

Journal of Geophysical Research: Atmospheres

Supporting Information for

Influences of Recent Particle Formation on Southern Ocean Aerosol Variability and Low Cloud Properties

Isabel L. McCoy[1], Christopher S. Bretherton[1], Robert Wood[1], Cynthia H. Twohy[2], Andrew Gettelman[3], Charles G. Bardeen[3], and Darin W. Toohey[4]

[1] Atmospheric Sciences, University of Washington, Seattle, WA, USA, [2] Northwest Research Associates, Redmond, WA, USA, [3] National Center for Atmospheric Research, Boulder, CO, USA, [4]Atmospheric and Oceanic Sciences, University of Colorado, Boulder, CO, USA.

Contents of this file

Additional Supporting Information (Files uploaded separately)

Movie S1

Text S1.

The instrumental setup for the CVI during SOCRATES was unique and facilitated an approximate volatility estimate. Normally, the CVI preferentially separates cloud droplets using a counterflow out the tip. For out of cloud, ambient aerosol measurements the counterflow is turned off. The CVI has two primary heaters that can affect particle volatility, one on the probe and one on the long sample line. The CVI probe was heated to ~50-60°C for the majority of the flights to evaporate water and prevent icing when sampling inside supercooled clouds. Because of the instrument and inlet configuration required on the GV, a 4.5m line heated to ~40°C was run between the inlet of the CVI and the instrument rack. The total residence time in the CVI probe and sample line is 2.3 seconds. During their passage through the heated probe and sample line, smaller, more volatile ambient aerosol particles are evaporated.

The result of this setup is that for the majority of flights during the campaign the instruments behind the CVI sampled only particles not volatile at ~50°C. During the second half of the campaign, the temperature of the CVI instrument was varied between ~25-60°C to allow for a more detailed investigation of the particle volatility observed. Since the CVI has two primary heated regions, the instrument (probe and tip) and sample line, and they behave differently when the heaters are turned off, the maximum of these three temperatures is used for estimating the volatility temperature (i.e. CVI tip, probe, and sample line). Because this analysis approach was not foreseen, the volatilization estimates produced are inexact but still useful for interpreting particle composition in the free troposphere.

Movie S1. Synoptic scale patterns influencing mid-tropospheric RPF identified air masses in the 72-hour period before sampling by RF07 (black line from Tasmania). ERA5 reanalysis maps include 700 hPa vertical velocity (colors) with a 700 hPa geopotential height contour of 2.9 km for reference (black contour). RPF trajectories (gray lines) with air mass locations (circles) colored by their altitude (white to purple, as in the ascent profiles in Figure 5a). Ascent of the first set of trajectories at ~60-hr occurs off the tip of Africa while ascent of the ~36-hr trajectories occurs off the coast of Antarctica, both driven by the advance of a warm-conveyor belt towards the south east (i.e. along the height contour).

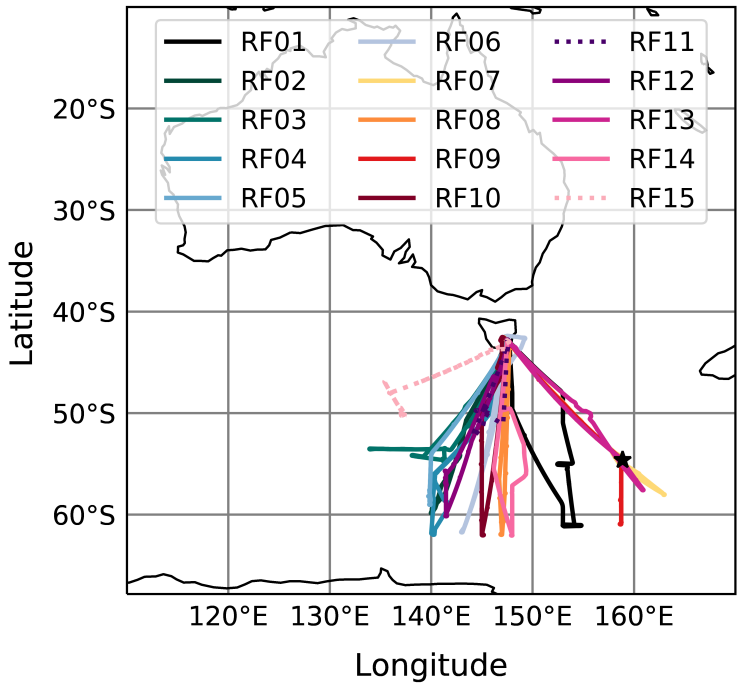

Figure S1. Research flight paths during SOCRATES (dashed lines for cumulus targeting flights, solid for standard modules). Macquarie Island, a coordinated site for ground observations as detailed in McFarquhar et al. (2020) is marked with a star.

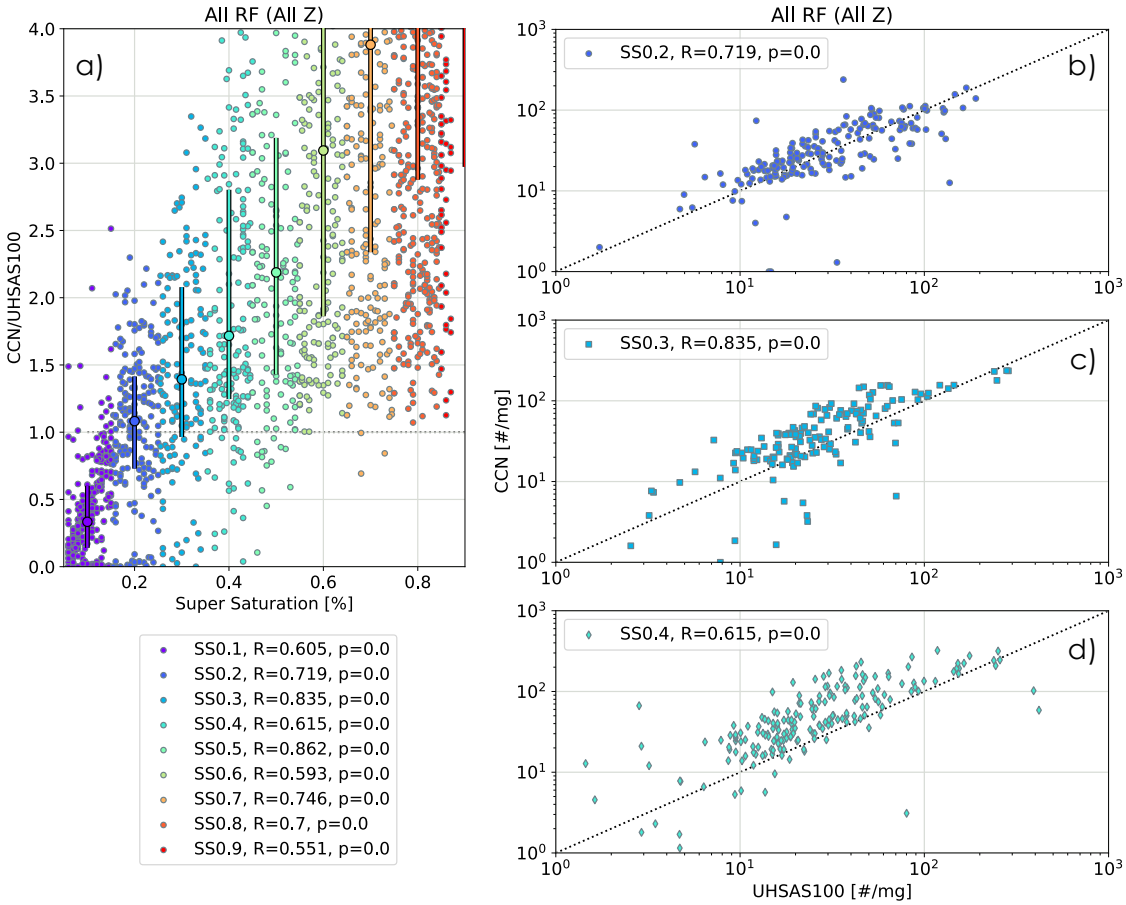

Figure S2. Relationship between scanning CCN (Sanchez & Roberts, 2018) and UHSAS100 during SOCRATES for all altitudes and samples available, binned by 1.5 minutes. (a) Ratios between CCN and UHSAS100 with correlation coefficients (legend) colored by supersaturation (SS). The three SS with ratios closest to 1 are shown separately as scatters: 0.2% (b), 0.3% (c), and 0.4% (d). SS of 0.2% is the best proxy for UHSAS100 as it has a ratio near unity and a significant correlation.

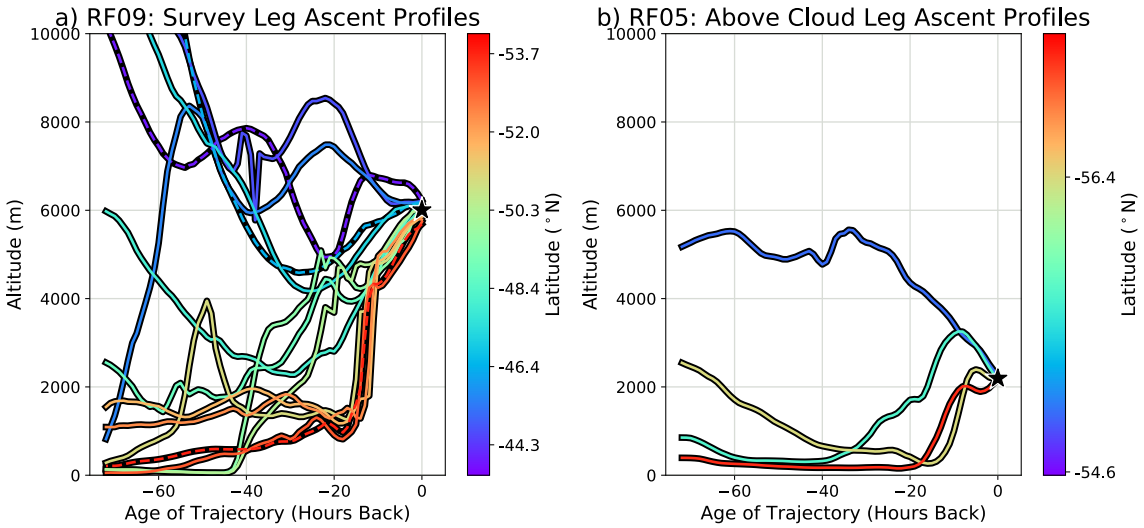

Figure S3. HYSPLIT 72-hour back trajectories of air masses initiated in 10-minute intervals corresponding to starred locations in Figure 2: (a) survey-leg sampling in the mid-troposphere during RF09, and (b) above cloud leg sampling during RF05. Lines are colored by latitude of sampled air along the GV flight path and match star locations in Figure 2. Trajectories that do not satisfy the criteria for RPF events ($CN_{Max10} < 2500$ mg^{-1}) are dashed.

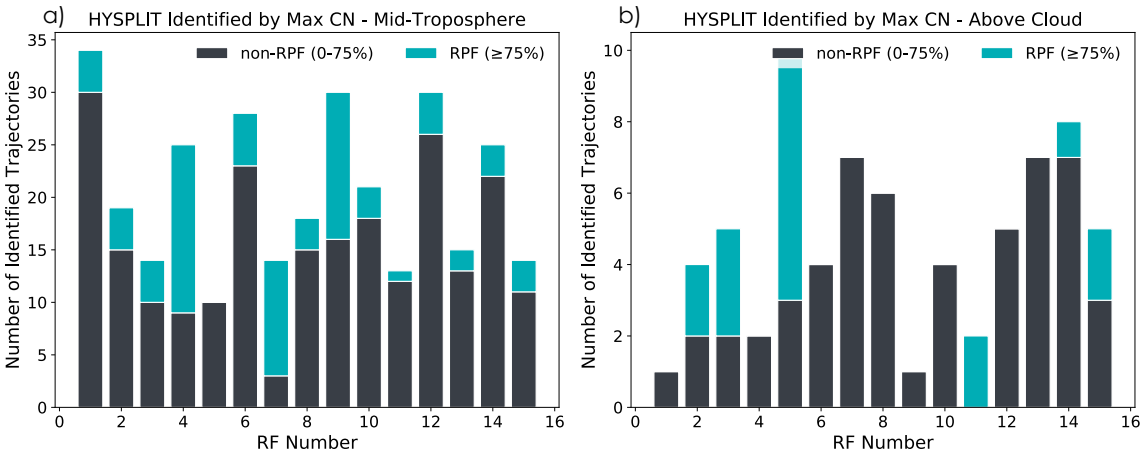

Figure S4. Number of RPF (blue) vs non-RPF identified HYSPLIT trajectories by research flight for trajectories initiated in the (a) mid-troposphere and (b) above cloud.

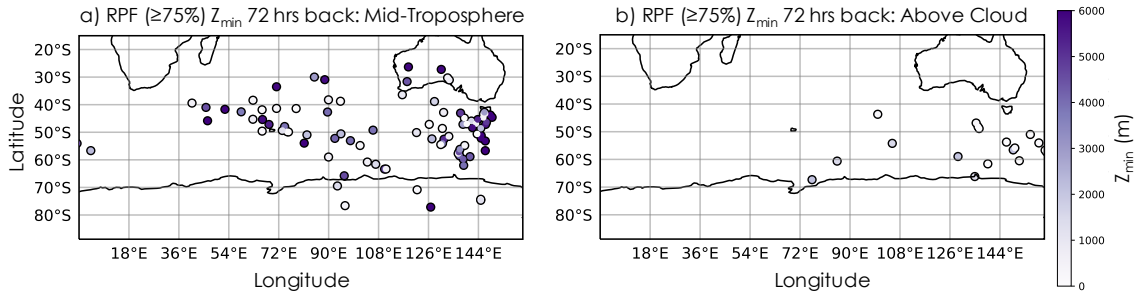

Figure S5. Location and altitude of minimum height that occurs over full 72 hours for RPF identified trajectories in (a) mid-troposphere and (b) above cloud.

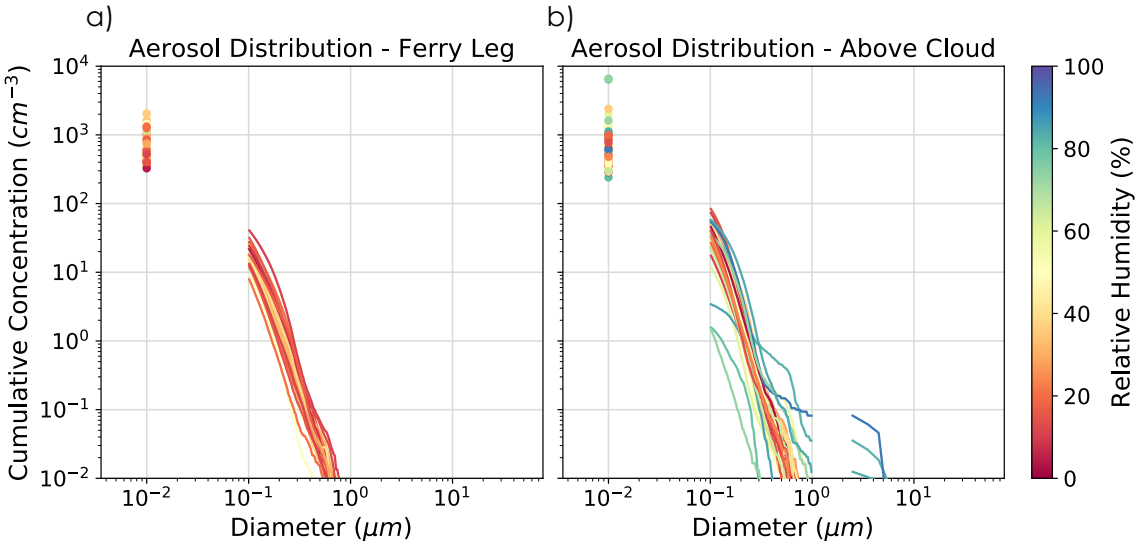

Figure S6. Median cumulative size distributions for each level leg in the mid-troposphere (a) and above cloud (b) sampled during the campaign. Each line is colored by the median relative humidity to indicate where near cloud contamination may be occurring. There are several instances of this in the above cloud sampling (b). However, the majority of the cumulative size distributions demonstrate the dominance of Aitken particles in the free troposphere (a, b). Note that concentrations are not adjusted for standard temperature and pressure.

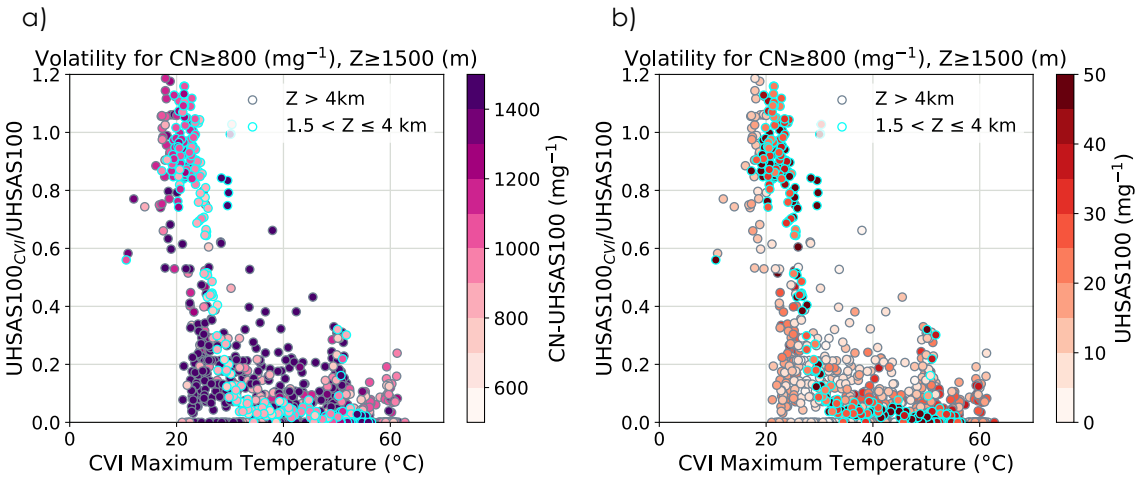

Figure S7. Volatility curves from CVI analysis as in Figure 7 but for the small number of accumulation mode particles captured in these Aitken-dominated samples. Accumulation mode volatilization is presented as the ratio between UHSAS100 and UHSAS100$_{CVI}$ versus the maximum temperature of the CVI instrument. Points are shown for CN ≥ 800 mg^{-1} and limited to free tropospheric samples (Z ≥ 1.5 km). Outline colors denote altitude of sample: mid-troposphere (gray) and above cloud (blue). Points are colored to estimate the number of particles in the Aitken mode (a, CN-UHSAS100, generally more in the mid-troposphere) and accumulation mode (b, UHSAS100, more above cloud). Note that accumulation number in these Aitken-dominated samples are rarely more than 30 mg^{-1} in mid-troposphere and increase only to ~50 mg^{-1} above cloud.

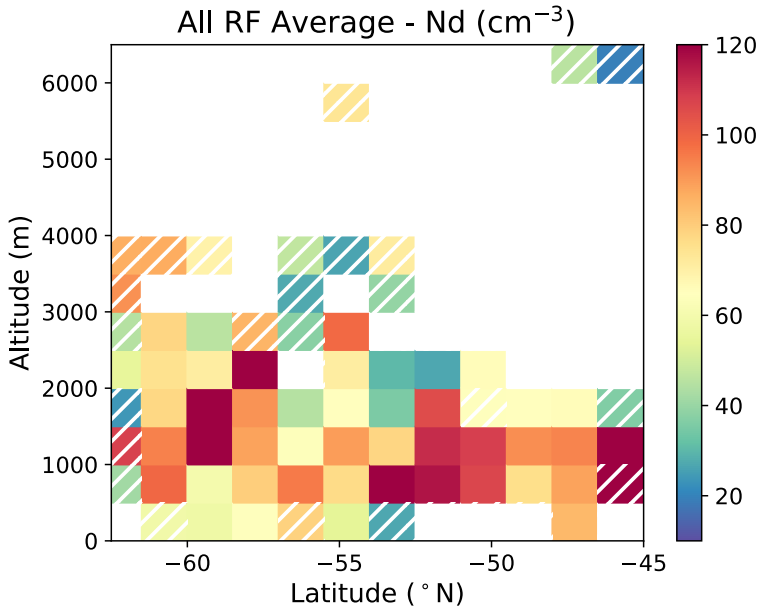

Figure S8. All flight average composite of binned flight medians (500 m x 1.5° boxes) for cloud droplet number concentration as in Figure 8d but using volume units (cm^{-3}) instead of standard temperature and pressure corrected units (mg^{-1}). Bins where 2 or less flights sampled are hatched to indicate inadequate sampling.

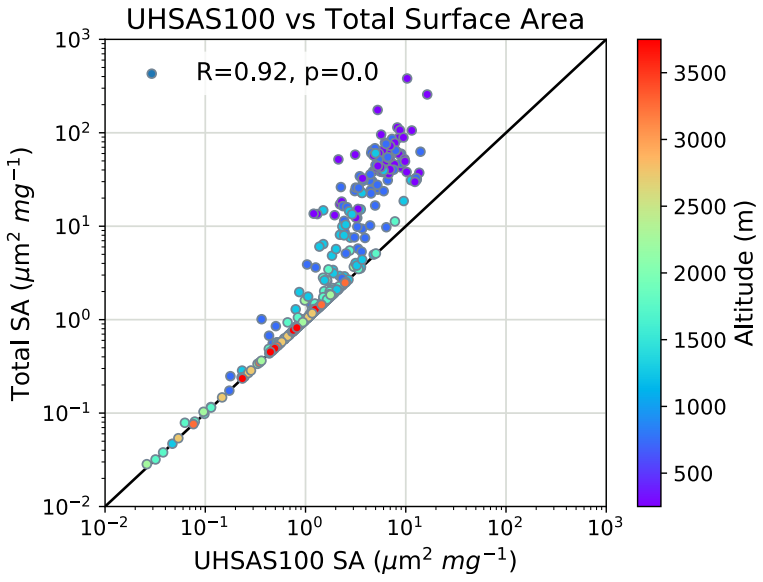

Figure S9. Total (CDP+UHSAS100) surface area vs. surface area computed from UHSAS100 alone for observations binned into 500 m x 1.5° boxes for each flight during SOCRATES. Points are colored by altitude. Only data in pristine (south of 45°S) from Z≤ 4 km are considered. A 1:1 line is included for reference along with the correlation coefficient and *p*-value for the log-log relationship.

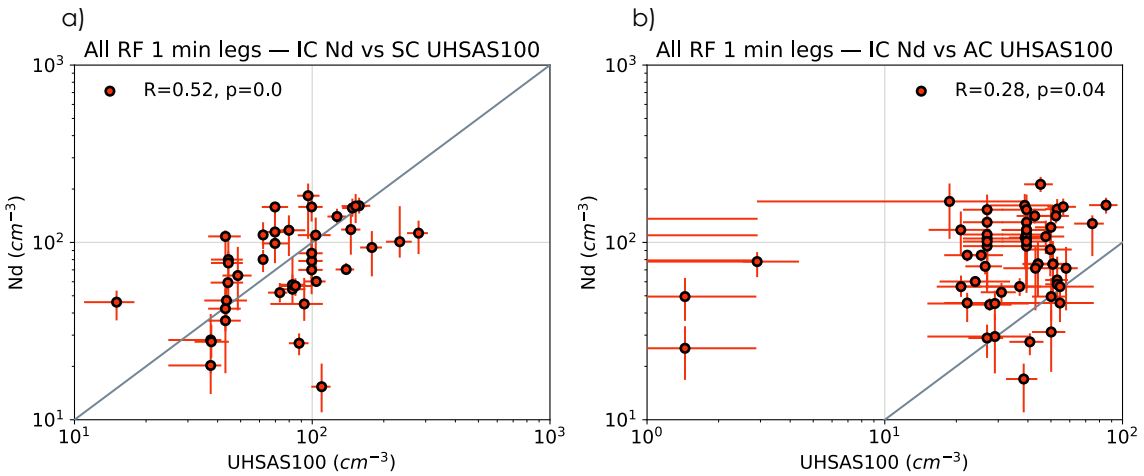

Figure S10. In-cloud median N_d versus nearest sub-cloud (a) and above-cloud (b) median UHSAS100 for SOCRATES level legs (≥1 min in length). Lines associated with each point are the 25th-75th percentiles across the level leg. A 1:1 line is included for reference as well as the correlation coefficient and p-values for each log-log relationship.

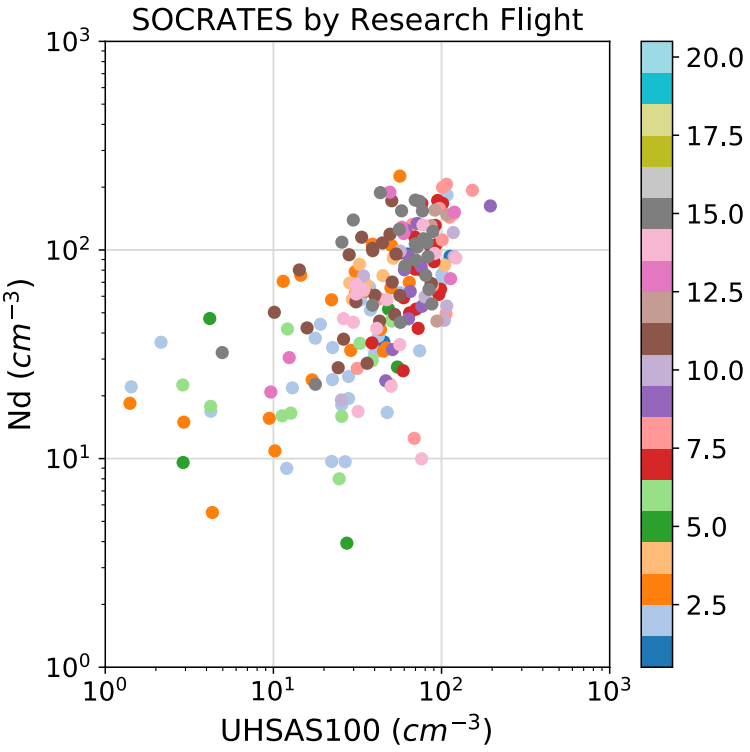

Figure S11. N_d versus UHSAS100 for SOCRATES data binned by 2 min x 50 m. Colors mark the research flight number and helps us to identify which flights have low N_d and/or low UHSAS100 occurrences.

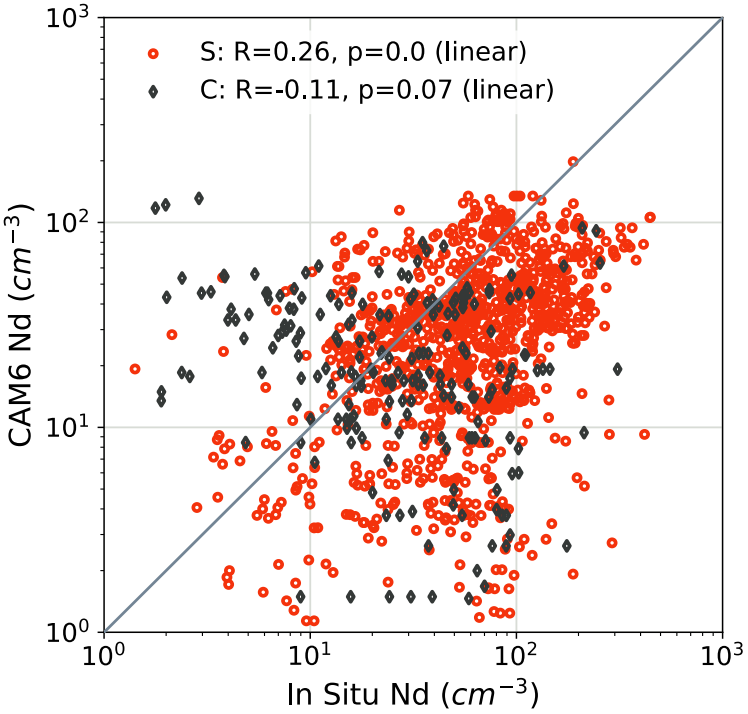

Figure S12. N_d comparison between CAM6 and in-situ samples binned by flight at 2 min x 50 m from CSET (gray) and SOCRATES (orange). A reference 1:1 line is included along with correlation coefficients and p-values computed for the linear relationship between CAM6 and observations. CAM6 over produces precipitation-depleted clouds ($N_d \leq 10$ cm^{-3}) relative to SOCRATES observations and are not collocated with actual observations for either CSET or SOCRATES.

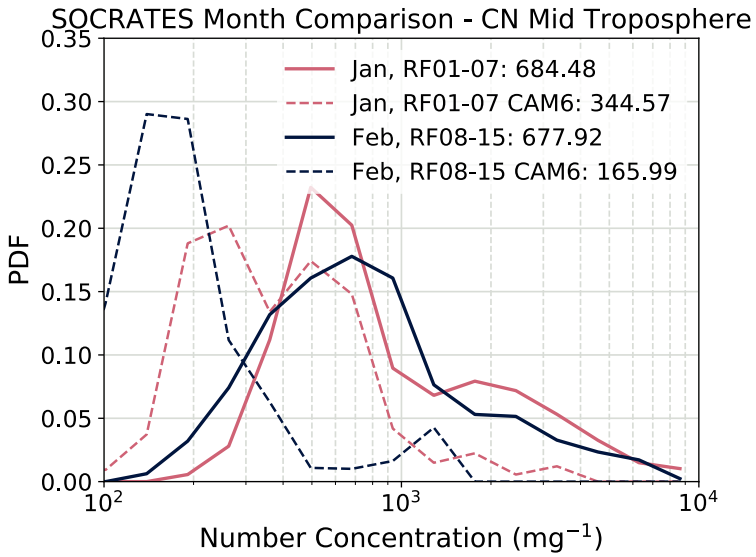

Figure S13. Observed CN number concentration in the mid-troposphere for January (RF01-07) and February (RF08-15) have similar pdfs (and similar sampling amounts), suggesting statistically consistent CN concentrations across these months. CAM6 matched CN has distinctly different PDFs for January and February, with February producing much lower CN than January and far too low relative to observations. Both CAM6 month pdfs under produce high concentrations of aerosol (CN ≥ 1000 mg^{-1}) relative to observations. Medians are provided for comparison.